ABSTRACT

Title of Thesis: COMPUTATIONAL FLUID DYNAMICS MODELING OF SHOCK TUBE GENERATED BLAST-INDUCED PRESSURE FIELDS ON THE HUMAN HEAD.

Rubbel Kumar
Master of Science, 2018

Thesis Directed By: Professor Elaine S. Oran,
Department of Aerospace Engineering

The increased use of explosives in military conflicts has been linked to an increase in the number of traumatic brain injuries (TBIs). Assessing the effectiveness of personal protective equipment to mitigate TBIs requires both the ability to replicate the pressure signatures caused by blast waves and an understanding of the interaction between blast waves and human bodies. Computational Fluid Dynamics (CFD) was used to understand the effect of varying different shock tube design parameters and to propose guidelines for selecting shock tube designs to accurately replicate blast wave pressure signatures representative of free-field explosive events. Additionally, a CFD model was developed to represent a shock tube built to mimic the primary overpressure magnitude and impulse loading on the human head surface as a result of free-field explosive events. This model

was used to aid in the understanding of flow within the shock tube, characterize the applied pressure loading to a bare head form, augment experimental findings to fully understand the influence of headborne systems on pressure applied to the human head, and support the design of optimized laboratory test methodologies to represent a broad range of free-field blast events.

COMPUTATIONAL FLUID DYNAMICS MODELING OF SHOCK TUBE GENERATED BLAST-INDUCED PRESSURE FIELDS ON THE HUMAN HEAD.

By

Rubbel Kumar

Thesis submitted to the Faculty of the Graduate School of the
University of Maryland, College Park, in partial fulfillment
of the requirements for the degree of
Master of Science
2018

Advisory Committee:
Prof. Elaine S. Oran, Chair
Dr. Alison B. Flatau
Dr. David R. Mott
Prof. Kenneth Yu

Acknowledgements

I would like to start by thanking my advisor, Dr. Elaine Oran, for her guidance and support during my graduate research. I would also like to thank the other members of my thesis committee, Dr. Alison Flatau, Dr. David Mott, and Dr. Kenneth Yu for their feedback on my thesis and their flexibility with scheduling my thesis defense.

A big thank you to my mentor, Dr. Ashish Nedungadi, for teaching me computational fluid dynamics, grid generation, bash scripting, and data visualization, and for getting me involved in the project that would ultimately become my thesis topic. Thank you to Roger Davis, Brad Marples, and Al Gronlund for your support and flexibility over these last four years as I completed my graduate degree part-time while working full time. Thank you to Katy Carneal for coordinating this work and all your feedback and support throughout the process. Also, thank you to Dr. Vanessa Alphonse for your help with finding prior research and John Clark for teaching me the experimental aspect of the program. A special thank you to Joan Murphy for your help navigating the public release process with tight deadlines.

Thank you, Tom, Aileen, Matt, and the rest of the Department of Aerospace Engineering for always being so helpful and for creating a welcoming environment throughout my undergraduate and graduate studies at the University of Maryland.

I would not be where I am today without the amazing support of my parents. Thank you, mom and dad, for sacrificing so much so that I could become a college graduate and pursue an advanced degree, and for teaching me to always work hard and

do my best. And a very special thank you to Sylvie for all your support throughout the past four years of completing my graduate degree—I know it hasn't always been easy!

Finally, this material is based upon work supported by the United States Army Natick Soldier Research Development and Engineering Center.

Table of Contents

List of Tables

List of Figures

1. Introduction

1.1. Background and Motivation

1.1.1. Improvised Explosive Devices

Detonation of improvised explosive devices (IEDs) is typically associated with shrapnel and fire, both of which lead to visible injuries. IEDs also produce blast waves that can lead to injuries that are superficially undetectable. The increased use of IEDs in military conflicts has now been associated with a major increase in the number of traumatic brain injuries (TBIs) [1]. The increased prevalence of this injury has led to a heightened need to investigate both the mechanisms by which the injury occurs and the need for personal protective equipment (PPE), such as helmet systems and goggles.

1.1.2. Blast Waves

To conduct these analyses effectively, it is important to develop well-characterized the blast overpressure signatures that represent relevant overpressure magnitudes and durations experienced by warfighters in theater, through either blast testing or laboratory-based methods. The Friedlander shock profile is a good target waveform to replicate through laboratory-based methods because it is a theoretical approximation and neglects the effects of reverb, secondary shocks, ground bounce, and reflections. The Friedlander blast wave profile is described by the modified Friedlander equation shown below, where P is the pressure, P_0 is the peak pressure, t is the time, t_d is the duration of the positive phase, and b is the exponential constant that controls the rate of decay [2].

$$P = P_0\left(1 - {}^{t}\!/_{t_d}\right)e^{-bt}/_{t_d}$$

Figure 1.1 shows a Friedlander profile obtained with a peak pressure, P_0, of 500 kPa, positive phase time-duration, t_d, of 10 seconds, and an exponential constant, b, of 1. A person subjected to this representative blast wave first experiences a sharp pressure rise due to the passage of the shock front, followed by an exponential decay, and finally a rarefaction wave [3]. The positive phase of the wave is the period between the initial pressure rise and the time the pressure first returns to ambient conditions, or the duration in which the pressure is positive. The positive phase is between 0 and 10 ms in Figure 1.1. Similarly, the negative phase of the wave is the period between when the pressure drops below the ambient conditions to the time the pressure once again returns to ambient conditions, or the duration in which the pressure is negative. The negative phase occurs after 10 ms in Figure 1.1.

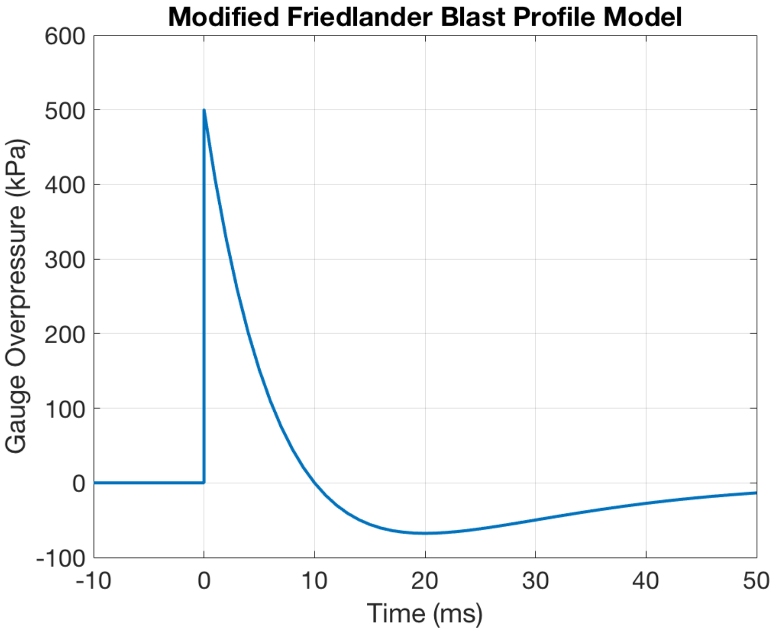

Figure 1.1: Friedlander wave profile with b = 1, P_0 = 500 kPa, and t_d = 10 ms

Although the generation of a Friedlander profile provides experimentalists with a reasonable approximation of the blast-overpressures experienced in theater, additional complexities such as reverb, ground bounce, buildings, vehicles, and other people exist in the field that may be difficult to replicate experimentally.

1.1.3. Free-field Testing

Free-field testing refers to the field testing of mannequins outfitted with pressure gauges and exposed to simplistic blasts caused by explosive detonation some distance and angle away. Free-field testing may better replicate real-world scenarios and provide more representative overpressure data than laboratory methods. Organizations such as the Naval Research Laboratory (NRL), Allen Vanguard, and the Johns Hopkins University Applied Physics Laboratory (JHU/APL) often validate computational models and other experimental techniques against data obtained through free-field tests [4]. A photograph taken from the experimental setup of a free-field test conducted by NRL and Allen Vanguard is shown in Figure 1.2.

Figure 1.2: Photograph of experimental set-up with two mannequins facing forward, toward the blast. Center pillar was a high explosive, which generated the blast wave once

detonated. Testing was conducted by Naval Research Laboratory and Allen Vanguard [5].

In addition to free-field testing, NRL has conducted computational fluid dynamics (CFD) studies modeling free-field tests and the blast's impact on bare and protected head forms where different combinations of protection (e.g., helmets, goggles or visors, and mandible protection) were used [5, 6]. Figure 1.3 is of a simple schematic showing the free-field test geometry modeled by NRL and Allen Vanguard.

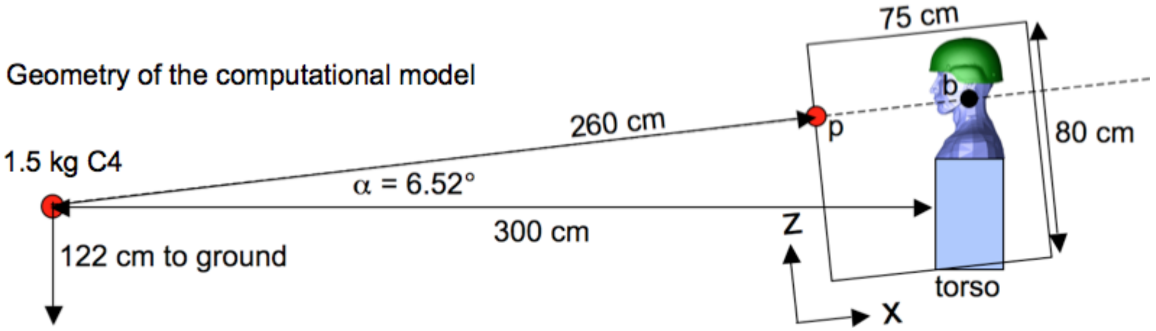

Figure 1.3: Blast geometry modeled in CFD for frontal blast impacts [5]

A key finding of NRL's research was that a particular type of protective equipment (e.g., visor) might decrease the overpressures at some locations, while simultaneously increasing the overpressures on separate regions of the head [6]. Figure 1.4 shows a summary of the pressure history results for front-facing blasts for four different PPE configurations [6].

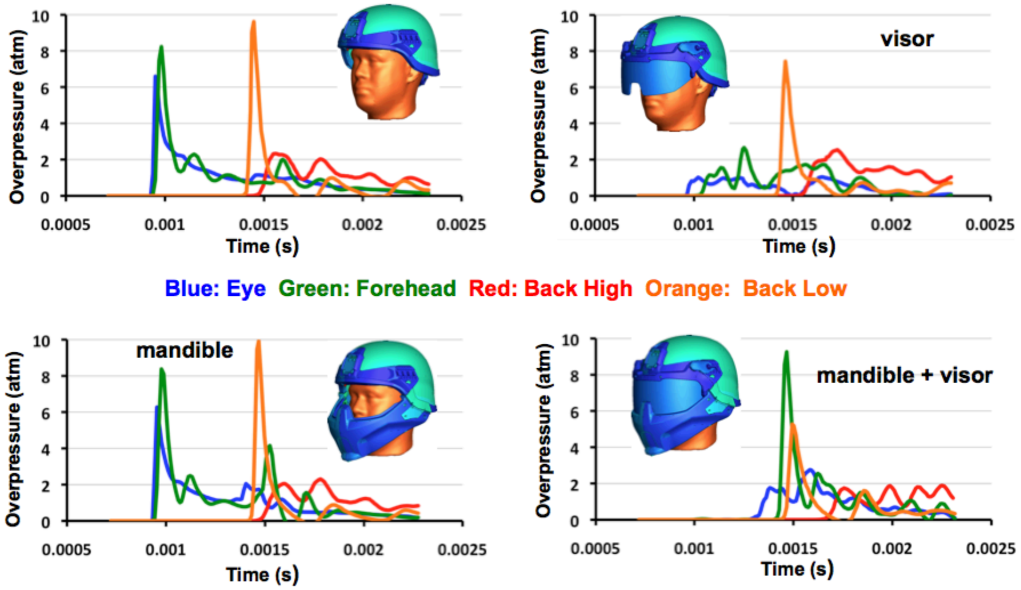

Figure 1.4: Pressure histories for front-facing blasts for four PPE configurations [6]

Unfortunately, free-field methods are costly, inherently limited in repeatability, and therefore not conducive to a large number of tests [7]. Laboratory test methods using shock tubes offer more controlled, repeatable, and less expensive platforms for assessing blast traumatic brain injuries (bTBI) and performance of PPE. Furthermore, previous research has shown specific shock tubes can generate blast signatures representative of free-field events [8].

1.1.4. Shock Tube Testing

Although compression-driven shock tubes have been validated as a method of generating representative blast waves [8], blast waves produced by shock tubes depend on a number of design parameters, including the driving gas, the driver (breech) length, and the membrane burst pressure, which is the pressure at which the membrane separating the pressurized driver section from the driven section bursts [9]. A simplified schematic of a constant diameter shock tube is shown in Figure 1.5. The driver section, which is filled with pressurized gas, is separated from the driven section by a membrane. Once the pressures in the driver section increase enough, the membrane will rupture and air will quickly escape into the driven section, forming a shock. The pressurized gas in the driver section is often referred to as the driving gas and the gas in the driven section as the driven gas.

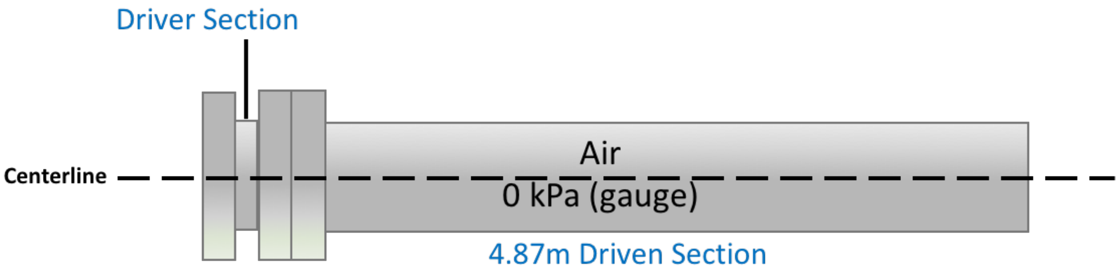

Figure 1.5: Simplified constant-area shock tube schematic

Reneer et al. (2011) conducted experiments using a multi-mode shock tube and showed how the use of different driving gases affected the pressure signature and the injuries to a rat brain in the test section [10]. Figure 1.6 shows the different rat brains after being exposed to blast waves that resulted from different driving gases [10]. The vascular damage appears to be more pronounced for brains exposed to blast waves when the driving gas was compressed air instead of oxyhydrogen [10].

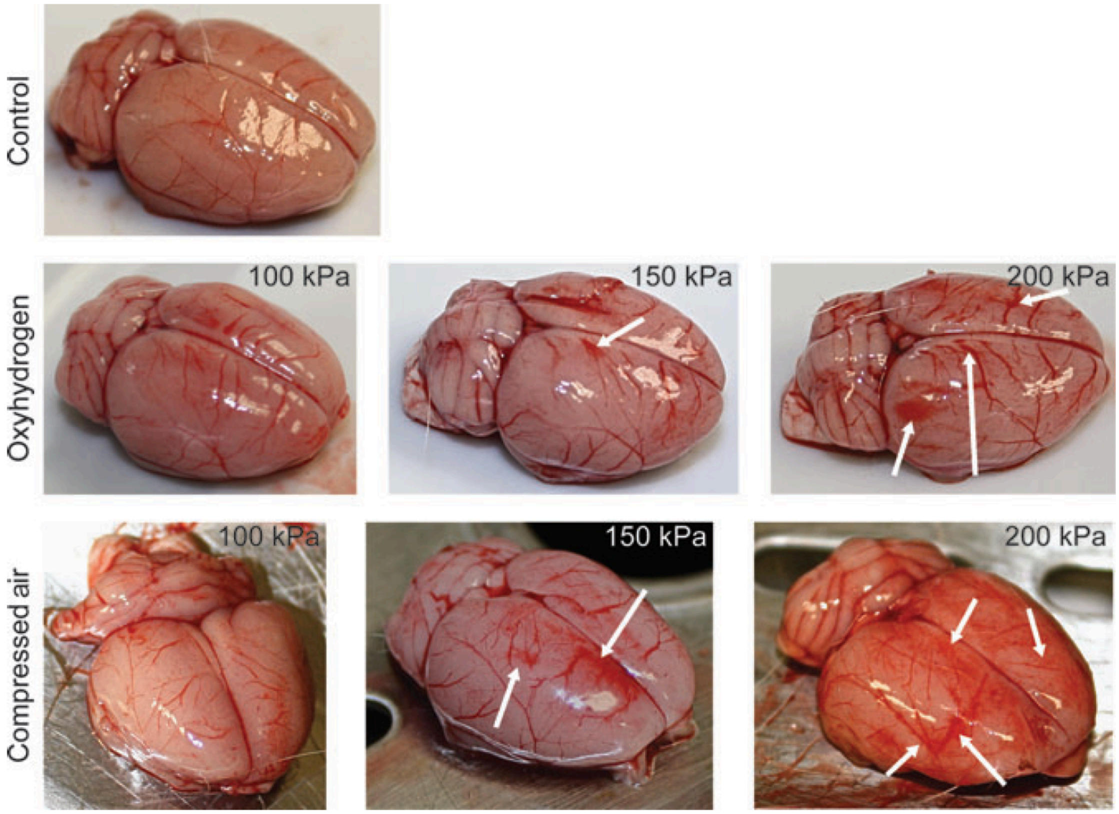

Figure 1.6: Representative photographs of the rat brains following exposure to different driving gases and at various peak overpressures. White arrows point to hematomas. [10]

Sundaramurthy and Chandra (2014) also studied the impact of different driving gases on the shock profile generated by a shock tube and conducted additional parametric studies that varied the shock tube breech length and burst pressure [9]. They concluded that a compressed-gas shock tube can be used to simulate primary blast injury for blast-induced neurotrauma studies.

Other researchers studied how flow properties differ inside and outside a shock tube to assess the validity of testing outside a shock tube, called "end-jet testing." Chandra et al. (2012) studied the shock evolution within and outside shock tubes, concluding that the placement of a test article outside of the open end of a shock tube exposed the test article to complex flow phenomena that were not representative of blast waves in the field [8]. Kuriakose et al. (2016) and Yu et al. (2014) also studied the effects of the test article's placement and whether end-jet testing provided representative results [11, 12]. Kuriakose et al. (2016) agreed with Chandra's conclusions, while Yu et al. (2014) concluded that end-jet testing was acceptable under specific constraints [8, 11, 12]. Specifically, Yu et al. (2014) concluded that testing inside is acceptable if the test article is placed at least 8-10 shock tube diameters down the driven section, and testing outside is acceptable if the test article is placed within ½ a tube diameter from the exit [12].

Shock tube testing has also been conducted with both surrogate bare and helmeted human head forms. The University of Nebraska-Lincoln (UNL) used conical shapes to model simplified head-helmet interfaces, such as the use of a cylindrical core to represent a head form, as shown in Figure 1.7 [13, 14].

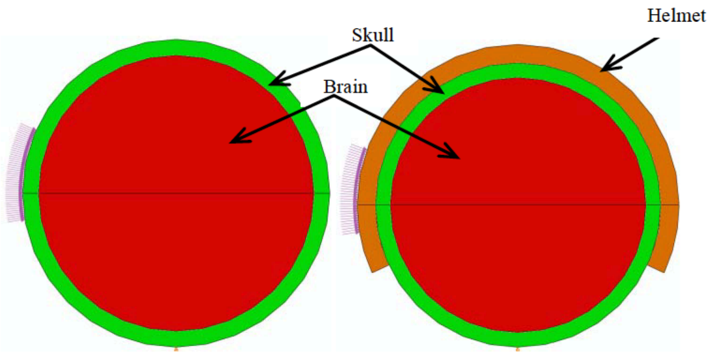

Model 1 : Skull and Brain

Model 2 : Helmet, Skull and Brain

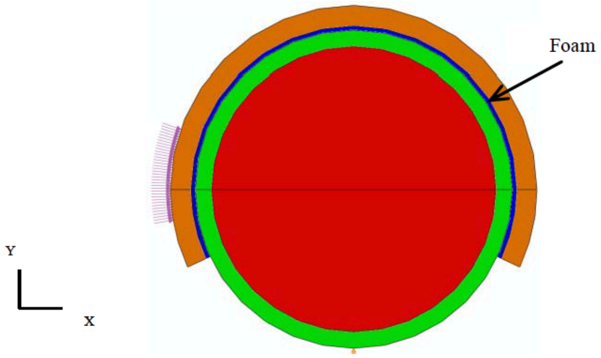

Model 3 : Helmet, Foam, Skull and Brain

Figure 1.7: Simplified head, brain, and helmet interface model [14]

UNL also conducted more detailed computational and experimental studies on the effect of blast waves on surrogate head forms [15, 16]. The University Carlos III of Madrid, National University of Singapore, and University of Melbourne conducted a joint computational study to understand the effect of helmet systems on human head responses under blast loading [17]. Similar to NRL, they used different combinations of PPE to understand how each combination influenced the head's response.

1.1.5. Blast Overpressure Simulation System

For a number of years, personnel at JHU/APL have conducted studies to improve their ability to replicate blast wave scenarios that cause injuries [4]. They used both shock tubes and free-field testing to characterize shocks generated by IEDs and assess the overpressures on surrogate head forms with and without PPE. Ultimately, JHU/APL built the Blast Overpressure Simulator System (BOSS) to improve their capability for laboratory testing.[1] Chapter 3 describes the development of a CFD model of the BOSS and its validation against experimental data obtained from the BOSS.

1.1.5.1. Geometry and Design

The geometrical and operational basis for the JHU/APL blast simulator was an existing Advanced Blast Simulator (ABS) with a 0.6096m x 0.6096m cross-sectional test area developed for use in small animal studies [18]. Key attributes of the original ABS system design preserved in the BOSS included the driver and transition sections with expanding cross-sectional area, which were found to be critical in replicating the wave dynamics of an expanding spherical blast including the negative phase and secondary shock [18]. The ABS design creates a fully-developed planar pressure exposure on test articles located at the test stations and an End-Wave Eliminator (EWE) following the test section that uses optimized venting to prevent unwanted reflection and rarefaction waves from the end affecting test conditions as well as mitigating noise and shock-flow efflux into the laboratory space [18]. Top-down and side views of the BOSS are shown in Figure 1.8.

---

[1] Experimental work was conducted by Joseph R. Andrist, Darrell A. Zinn, and John A. Clark at JHU/APL. The following information about the BOSS was provided by John A. Clark.

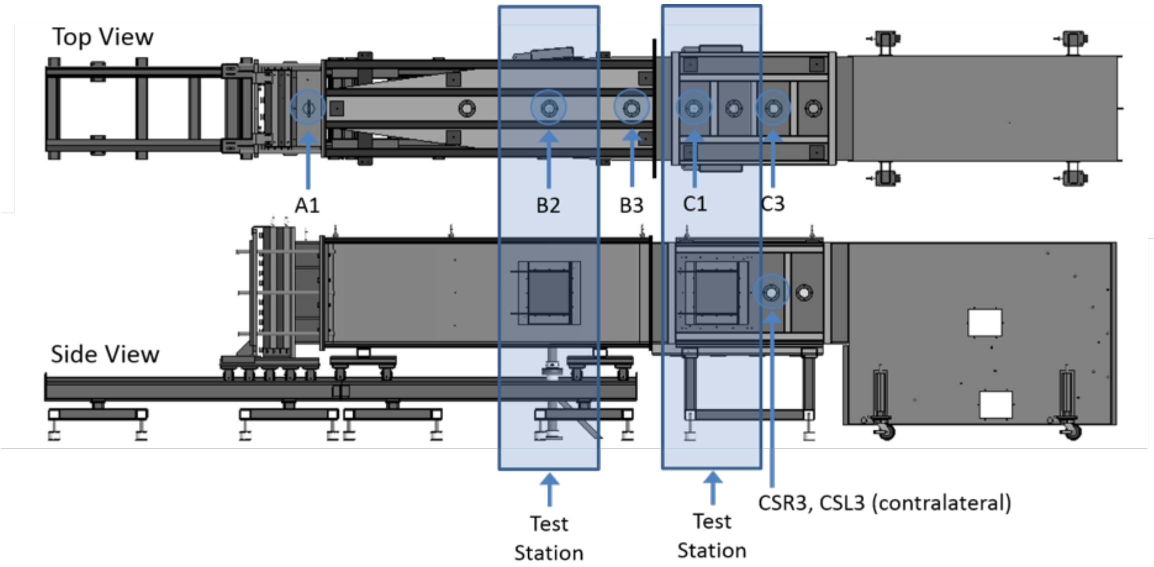

Figure 1.8: Top-down and side views of BOSS. Two potential test-section locations shown.

The BOSS is operated using compressed bottled gas that is rapidly filled into the driver section. The driver section can be filled with either mixed air or helium gas depending on the desired downstream pressure signature during system operation. Tests have been conducted using standard mixed air or Helium as the driving gas. Ambient air was always used as the driven gas.

During system operation, the diaphragm membrane materials are clamped at the junction of the driver and driven sections. The diaphragm-clamping frame was outfitted with six book bolts used to hold the two sections together while six 20-ton hydraulic rams evenly applied pressure to clamp the diaphragm during testing. The rupture characteristics of the diaphragm materials directly influence the waves created by the laboratory blast simulator system; therefore, it is important to get clean, complete, and consistent ruptures to produce repeatable data with minimal artifacts in the pressure-time histories. The mode of material failure (e.g., brittle vs elastic, rupture speed, failure patterns and direction) all influence the validity, duration, and repeatability of the waveforms.

The transition section provides a gradual, sigmoidal-shaped transition from the relatively narrow exit of the driver section (0.2286m width) to the full-width test section (0.9144m width) over the length of 3.048m. The expanding shape of this section ensures that a fully developed planar overpressure shock front is formed downstream of the diaphragm after the membrane bursts.

Two locations in the blast simulator system were selected to install test fixtures and instrumentation to support full helmeted head and neck evaluation. These locations have sufficiently large cross sectional areas and planar flow profiles to allow the idealized pressure signatures formed in the transition section to arrive at the test apparatus with a planar exposure and minimal artifacts.

1.1.5.2. Testing Procedure

The system requires two individuals to operate. Test articles and desired instrumentation are prepared and placed in the appropriate test location within the system as the first step. Next, membrane materials are carefully loaded between the diaphragm clamping frame and downstream ambient sections to ensure there are no creases of the material, and pre-clamping is achieved by manually tightening the book bolts. Once this is achieved, the hydraulic rams are used to apply an evenly distributed clamping pressure until the diaphragm is held in place with approximately 140 klbf of force. For safety purposes, both manual and computer controlled valves are used to fill the driver section with gas at a constant rate until the membrane bursts. Custom-built LabVIEW software allows the operator to monitor and control the supply and driver pressures while remotely initiating the test sequence.

A number of sensors are used during testing with the BOSS. These sensors were chosen for their high resonance frequency, high response rate, and their appropriate pressure sensing range and form factor. The wall gauges are mounted flush with the inner surface of the BOSS walls. Pitot-static gauges are mounted on the inertial frame at the test locations and are used to measure pressure in the center of the tube.

The BOSS is currently outfitted with a total of 15 sensor ports on the top and side walls to measure the pressure flow characteristics during operation. This includes one port in the driver section, three ports in the top wall of the transition section, one port on the right side of the transition section, and five ports each on the top and side walls of the test section, respectively. The current ports contain pressure sensors (Model HKS-375-100SG, Kulite Semiconductor Products, Inc., Leonia, NJ, USA), but can be modified to remove instrumentation or be replaced with clear windows for high-speed video at these locations. These sensor ports can be seen in top-down and side views of the BOSS apparatus in Figure 1.9.

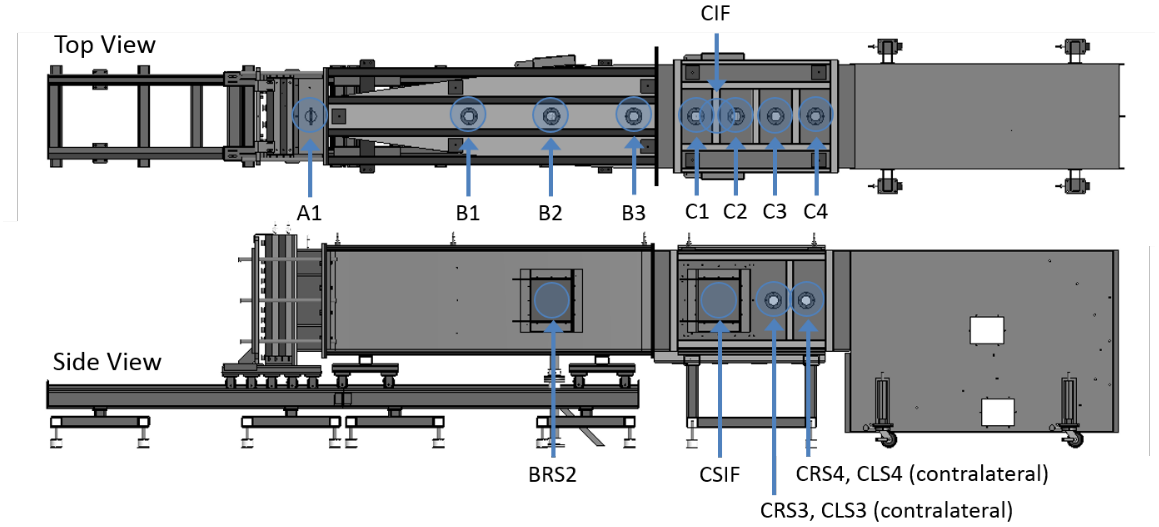

Figure 1.9: Current wall sensor port location in the BOSS (A = driver section, B = transition section, C = test section, R = right wall, L = left wall)

In addition to the wall pressure data, pressure can be characterized in the center of the system via a modified Pitot-static probe fixture containing forward and rearward facing pressure gauges to capture total (forward-facing) and static (rearward-facing) overpressure, and a disc gauge to capture static overpressure. This Pitot-static gauge was designed and fabricated for use within the BOSS (Figure 1.10). This consists of three pressure sensors (Model 113A36, PCB Piezotronics, Depew, NY, USA). Two of the pressure sensors are mounted with the sensing surfaces perpendicular to the flow, one facing forward and the other facing rearward. The third pressure sensor measurement surface is oriented parallel to the flow; a plastic disc with a flat surface ensures zero flow velocity at this location. The original disc was fabricated out of aluminum but allowed vibration noise to be picked up by the pressure gauge, switching to a rapid-prototyped plastic disc alleviated the issue. This Pitot-static gauge is mounted within the flow field of the BOSS as shown in Figure 1.10, and measures stagnation and static overpressure in the center of the tube. The potential locations of this gauge are the two test stations shown in Figure 1.8.

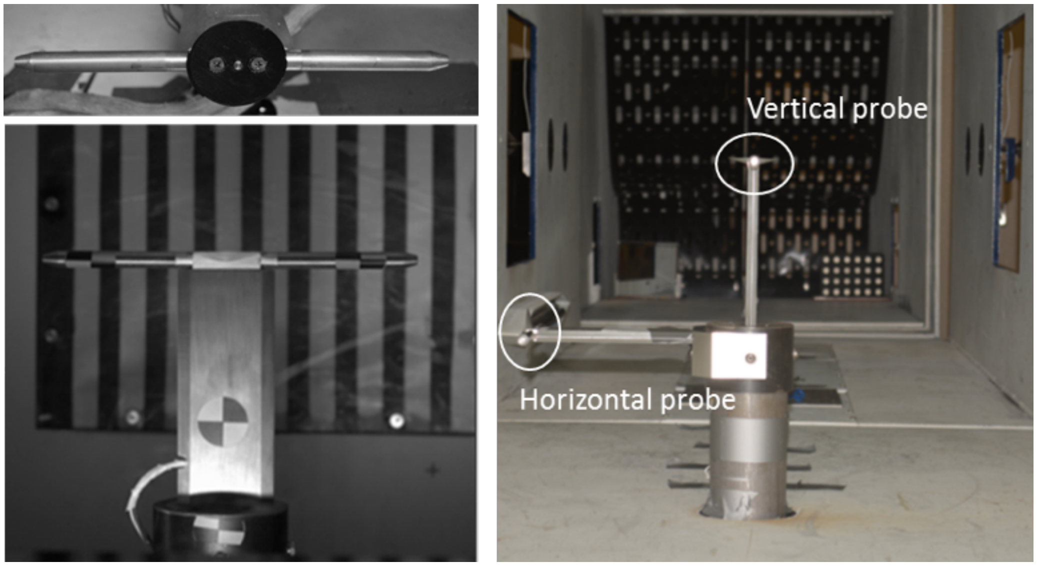

Figure 1.10: Custom Pitot-static gauge mounted on the inertial frame

1.1.5.3. Data Acquisition

All data were recorded at 500 ksps using a high-rate data acquisition system (Model 801, DEWETRON GmbH, Grambach, Austria). High-speed video[2] was taken at a frame rate of 20-25 kfps. Short videos were saved at the full frame rate to observe the arrival of the shock front and its progression around the headform. Longer videos were saved at a decimated frame rate to observe the headform kinematics.

1.2. Contributions of Thesis Research

The first objective of this research was to demonstrate the ability to use CFD to accurately predict the overpressures inside a shock tube. Then, CFD was used to corroborate the results of other researchers by reaffirming the ability to use shock tubes to generate pressure signatures that are representative of blast waves. However, this work focused on the evolution of the blast wave as it traveled down the shock tube for all shock tube designs that were studied instead of assuming a single test section location as was done for previous work. Parametric studies were performed with CFD to characterize the primary overpressure blast environment created from a variety of laboratory shock tube designs and understand the effects of varying the membrane burst pressure, driver length, and driving gas. The results from these analyses are provided in this thesis and can be used to inform future shock tube design and experiments to ensure the generated pressures are representative of blast waves.

---

[2] Video taken by Phantom V1611, high-speed camera from Vision Research, Inc., Wayne, NJ, USA

Additionally, a CFD model was developed to facilitate assessing the effectiveness of PPE. As part of the modeling process, a new bulging diaphragm model was developed to improve agreement of CFD-based pressure signatures with experimental measurements. Then, CFD was used to characterize the overpressures on bare and helmeted head forms for frontal, side, and rear impacts and assess the effectiveness of helmets for reduction of overpressures on the human head. CFD allows for computation of the overpressures throughout the shock tube and across the entire head form, whereas experimental studies provide results at only finite locations.

1.3. Overview of Thesis

This thesis is organized into four chapters. The first portion of this thesis relates to the characterization of shock tubes and the assessment of their ability to replicate free-field blast wave signatures. The second portion of the thesis focuses on validating a computational fluid dynamics model of a blast wave simulator and a head form test article against experimental data. The remainder of the thesis examines the effect of a nominal helmet geometry on overpressures on various portions of the head under different blast loading conditions.

Chapter 1: Introduction. This chapter presents an overview of the background and motivation for studying blast wave pressure signatures and shock tubes as a means of generating them. It provides necessary background on prior research on shock tubes and the effect of PPE on the human head. It also covers the objectives of the present research.

Chapter 2: Using Gas-Driven Shock Tubes to Produce Blast Wave Signatures. This chapter describes the characterization of constant-diameter shock tubes as key design parameters are changed, including membrane burst pressure, driver length, and driving gas.

It establishes the validity of using gas-driven shock tubes to produce blast wave signatures, forming the baseline for the remainder of the research.

Chapter 3: Assessment of Helmet Effectiveness against Blast Waves using Computational Fluid Dynamics Simulations of Gas-Driven Shock Tubes. This chapter establishes the validity of a CFD model of a custom blast wave simulator system by comparing pressure signatures at key locations in the shock tube to measured experimental data. Overpressures measured at select locations on bare and helmeted head forms serving as test articles are also compared between the CFD simulations and experimental data. Once the CFD simulations are validated, the remainder of this chapter assesses the effect of a nominal helmet on predicted head form overpressures under different impact orientations: frontal impact, side impact, and rear impact.

Chapter 4: Conclusions. A summary of observations and key findings from the previous chapters are provided. Contributions of this work and suggestions for future work are also discussed.

2. Using Gas-Driven Shock Tubes to Produce Blast Wave Signatures

2.1. Introduction

The objective of the work described in this chapter is to use computational fluid dynamics (CFD) simulations to show whether or not shock tubes can be used to generate pressure signatures that are representative of blast waves. Parametric studies were performed to characterize the primary overpressure blast environment created from a variety of laboratory shock tube designs. Studies were conducted to understand the effects of varying the membrane burst pressure, driver length, and driving gas. Conducting CFD simulations is less expensive, faster, and therefore better suited for the parametric studies than building an array of modular shock tubes to conduct laboratory experiments. The results from these analyses can be used to inform shock tube design and experiments to ensure the generated pressures are representative of blast waves.

2.2. Materials and Methods

The shock tube in this study consists of a high-pressure region (the driver section), separated by a diaphragm from a low-pressure region (the driven section). Depending on the application, the driver section may be at a different temperature and filled with a different gas than the driven section. When the diaphragm ruptures, a normal shock travels into the driven section and an expansion wave travels into the driver section [19]. For the current study, a constant-diameter shock tube was modeled with a driver that was allowed to vent to the atmosphere (farfield). No test article was modeled so shock tube conditions were considered unobstructed.

2.2.1. Shock Tube Geometry and Baseline Mesh Description

The shock tube geometry for these studies was a 0.1524 meter constant-diameter shock tube with a 0.1524 meter long driver section and a 4.87 meter long driven section. The computational mesh was generated in 2D using the commercial mesh generation software, Pointwise[3]. Pointwise can be used to create structured, unstructured, overset, and hybrid meshes. In this case, Pointwise was used to create a mesh with only quad elements. The mesh was created such that the bottom edge was a symmetry plane and the overall geometry was defined as 2D axisymmetric to model a circular cross section for the shock tube. Figure 2.1a shows the overall mesh of the shock tube, and Figure 2.1b shows a detailed view of the end of the driven section (highlighted in beige) with a small gap modeled between the shock tube wall (highlighted in red) and outside environment. This gap was modeled to give the shock tube wall a finite thickness while still allowing the exiting flow to turn the corner. A grid resolution study was conducted using the baseline mesh shown in Figure 2.1, a coarser mesh, and a finer mesh to ensure the results were grid independent.

---

[3] The software Pointwise and more information about it is available at www.pointwise.com

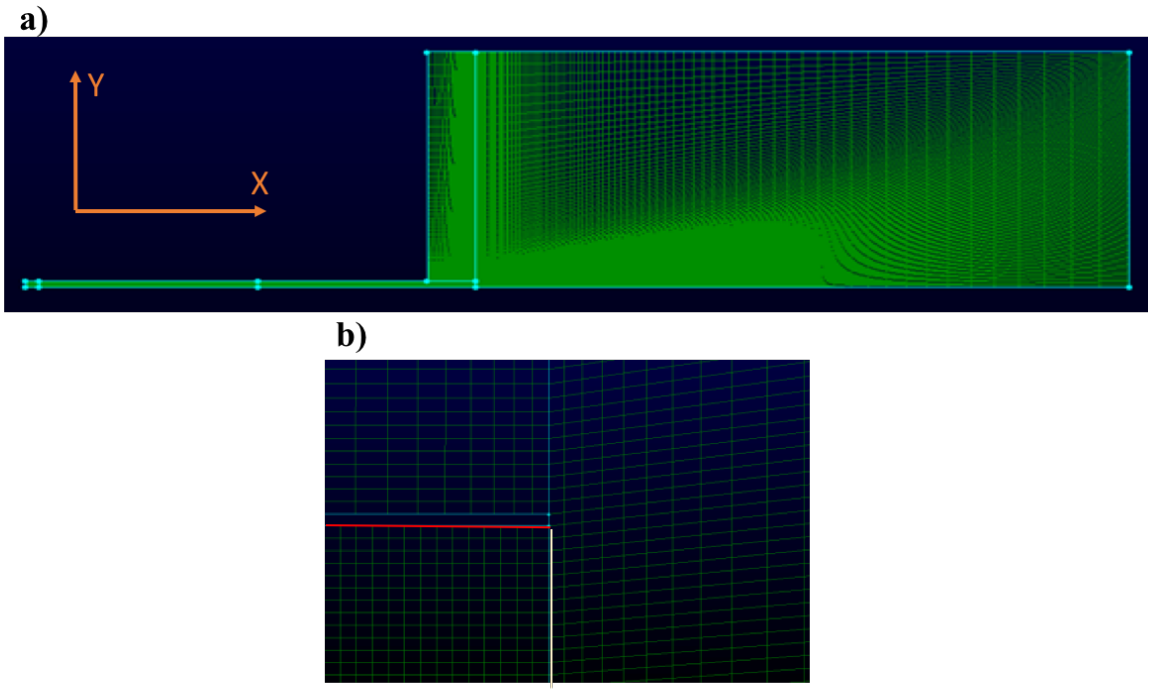

Figure 2.1: (a) Shock tube baseline computational mesh with (b) zoomed-in view of interface between shock tube driven section and outside environment

2.2.2. CFD Solver and Settings

CFD++[4] (version 15.1.1.u6), a commercial CFD solver developed by Metacomp Technologies Incorporated, was used for all the simulations described in the following studies. CFD++ is a versatile and generalized code that can solve the one, two, or three-dimensional, steady or unsteady, incompressible or compressible Reynolds-Averaged Navier Stokes (RANS) equations. The code's ability to include multiple species of gases was utilized for some of the parametric studies performed as part of this analysis. The code also has the ability to solve the Euler equations that describe inviscid flows. The code uses

---

[4] The software CFD++ and more information about it and about Metacomp Technologies Incorporated can be found at www.metacomptech.com

a finite volume formulation, a total variation diminishing scheme for spatial discretization, an implicit time-stepping algorithm for time discretization, and a modified Roe's Riemann solver for updating cell averages in time [20].

For the work described in this report, all simulations were set up to solve the two-dimensional (2-D) axisymmetric, unsteady, compressible fluid equations. For each time-step and grid cell, the code solves four 2-D conservation equations: mass, x-momentum, y-momentum, and energy. One or more additional equations are solved when a turbulence model is used and no additional equations are solved when the flow is modeled as inviscid.

When solving for flows with multiple species, additional N-1 equations are required, where N is the number of species. The study described in 2.4.3 was conducted to understand the effect of the driver gas on the pressures. At most, two species (air and helium) were modeled as one driver gas mixture, so one additional equation was solved for those simulations.

The flow through a shock tube is unsteady. The implicit (backward Euler), dual time-stepping algorithm was used to advance the solution from one physical time-step to another. At each global iteration (or time-step) the dual time-stepping algorithm iteratively solves the governing equations for a predefined number of inner iterations or until a predefined convergence criterion is satisfied. For simulating unsteady flows, the selection of the physical time-step is critical and depends on the velocities in the flow and the size of the smallest grid cell. If the time-step chosen is too large, the flow solution could become unstable and unphysical. If the time-step is too small, then the overall simulation (wall-clock) time can become very large. These issues are exacerbated when dealing with complex flows because of the need to have computational grids with many computational cells. A time-step study (not described here for brevity) was conducted for each candidate grid. Most cases were conducted to achieve at least 15 milliseconds of flow time. The inner iterations were set to 20 to achieve a convergence of two orders of magnitude. Early in the simulations, the code required 15-20 inner iterations to reach convergence; however, after the initial high-gradient transient flow decays, only 6-7 inner iterations were required for convergence.

2.2.3. Initial and Boundary Conditions

Each CFD simulation requires initial conditions (ICs) and boundary conditions (BCs). Here, the driver section was initialized with the driver gas at a given pressure (burst pressure) of 689.476, 1034.214, or 1378.951 kPa. The remaining ICs are shown in Table 1.

Table 1 Initial Conditions

Region	Absolute Pressure (Pa)	Temperature (Kelvin)	XYZ Velocity (m/s)
Driver	Burst Pressure	295	(0,0,0)
Driven	101325	295	(0,0,0)
Farfield	101325	295	(0,0,0)

At all solid surfaces (shock tube walls), boundaries were assumed isothermal. At the farfield boundaries, characteristic inflow/outflow conditions were applied with pressure and temperature set at 101325 Pa and 295 K, respectively. Most simulations were conducted assuming a symmetry in the Z = 0 plane. For these simulations, a symmetry BC was applied, where the normal (to the symmetry) component of velocity is zero. The symmetry BC acts as an inviscid wall BC, where only tangential flow is allowed. All simulations were conducted using a 0.1524 meter long driver section, a gauge burst pressure of 1034.214 kPa, and Helium driver gas unless otherwise noted.

2.2.4. Data Analysis and Post-Processing

Selected locations, shown in Figure **2.2**, along the shock tube centerline and the top wall were used to probe the flow. Data at these locations were taken at every time-step in order to find the pressure history at each probe location, and the maximum pressure at each location was calculated. The time at which this peak pressure occurs, t_{pmax}, was also recorded. Flow-field contours of the symmetry plane were saved every 100 time-steps.

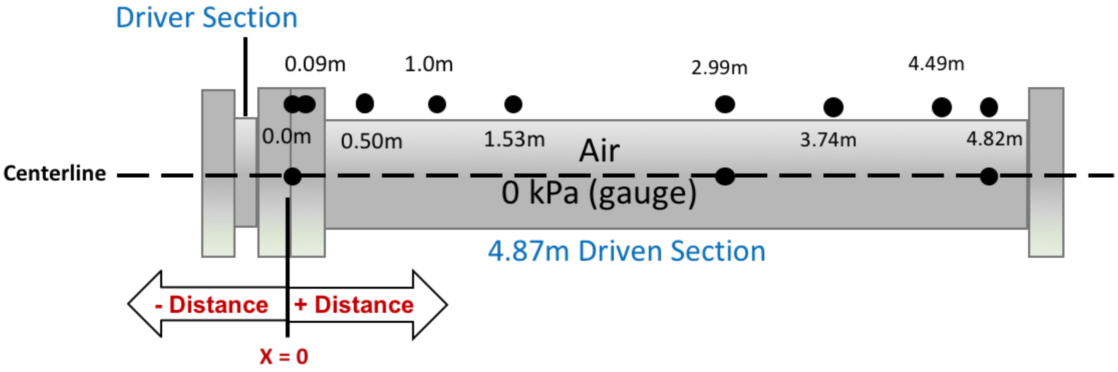

Figure 2.2: CFD schematic and probe locations

2.3. CFD Pre-processing: Time, Mesh, and Turbulence Model Independence

Mesh and time resolution studies were conducted to ensure that all results were mesh and time independent. An under-resolved mesh would artificially dissipate the shock, and a time-step that is too large could reduce the stability of the simulations leading to spurious oscillations, particularly near discontinuities such as shocks (Gibbs phenomena)

[21, 22, 23]. Similarly, a mesh that was too coarse would be unable to resolve the shock, and a mesh that was too fine would increase the simulation's runtime significantly. Because the flow along the shock tube centerline was of more interest than the flow near the wall where the effects of viscosity are more significant, the inviscid equations were solved and the mesh resolution was only varied within the tube and in the axial direction. After mesh-independence and time-independence studies were completed, a turbulence-model study was also conducted to ensure viscosity did not significantly change the results. The driver section was initialized with helium (He) for these studies. Pressure traces were compared for each simulation at two separate probe locations: 1 meter and 4.82 meters downstream from the driver/driven intersection. These two locations were chosen to compare the effect of design parameters on both the initial shock formation and the shock decay with distance.

The studies found that regardless of the computational mesh used, the time of arrival for the shock and maximum peak pressures remain within two percent for each of the simulations. A mesh containing approximately 94,000 computational cells was grid and time-step independent when using a time-step of 1 μs. The turbulence models did not significantly impact these results. The impact to shock arrival time is less than 1% and the effect on peak pressure is less than 5%. Therefore, the remainder of the simulations were conducted assuming an inviscid flow field to reduce the average simulation runtime. On average, simulations took three hours to run.

2.4. Results

2.4.1. Burst Pressure Study

In a laboratory experiment, a burst pressure study is one that tests the effect of the choice of the membrane on the pressure history. Different types of membranes burst at different pressures and, thus, the relation between the burst pressure and test-section peak pressure is observed. For our studies, it is necessary to understand the effect of membrane burst pressure on the positive phase duration of the wave. If the positive phase duration increases with the peak pressure, the overall impulse may increase significantly compared to a situation where the peak pressure increased and the positive phase duration did not.

The results of the burst pressure study, shown in Figure 2.3, show that the peak pressure increased as the membrane burst pressure increased, but the recovery percentage, P_{Peak}/P_{Burst}, decreased as the burst pressure increased. Furthermore, the rate of decay as the wave travels downstream is higher as the burst pressure increases. Finally, the higher burst pressures do increase the positive phase duration of the wave, suggesting that the impulse will be greatly increased.

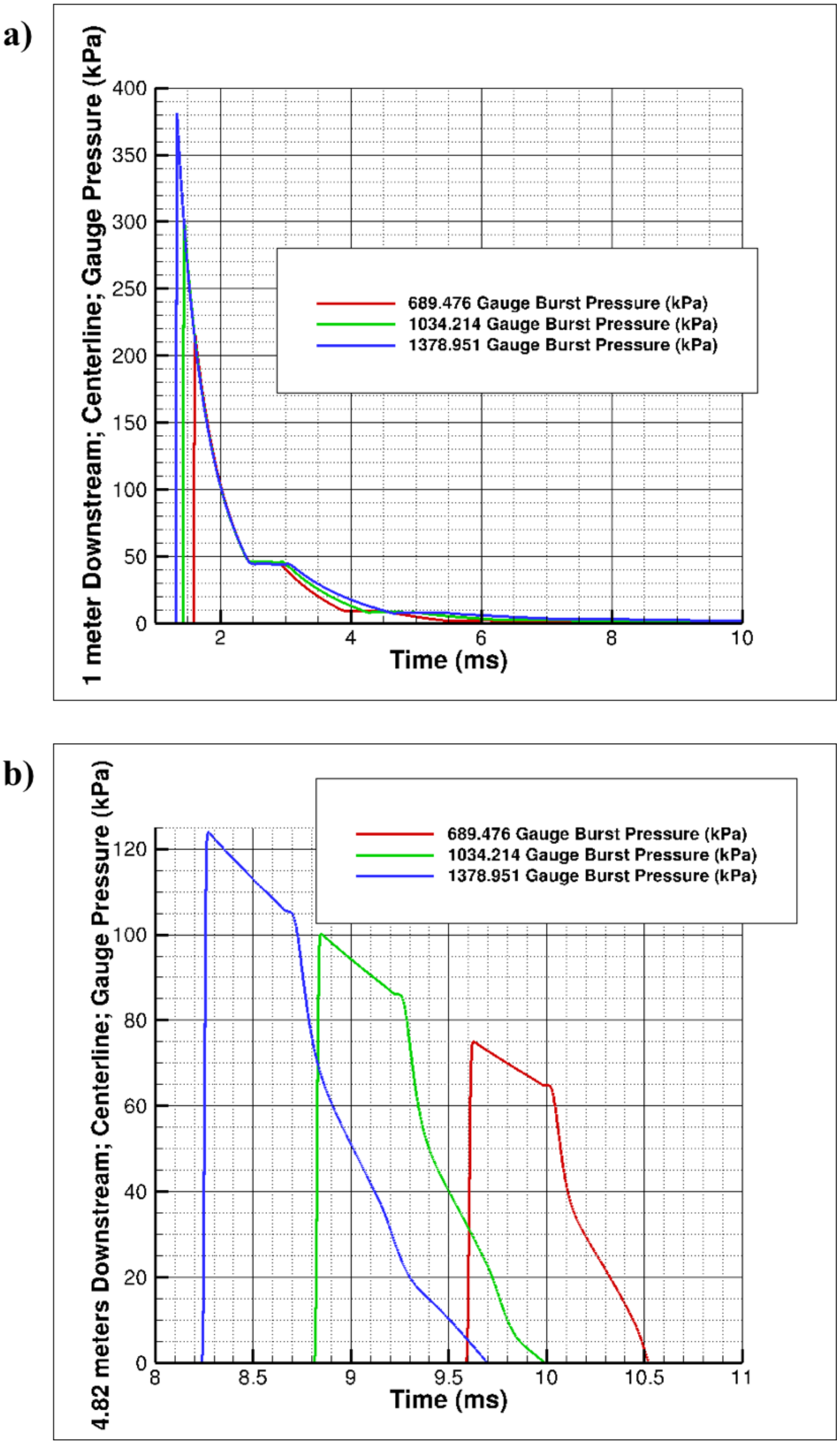

Figure 2.3: Burst pressure study; (a) 1 meter and (b) 4.82 meters downstream of driver/driven intersection

2.4.2. Driver Length Study

A study was conducted to examine the effect of different driver lengths on the shock evolution. Pressure traces were compared for this study at two separate probe locations: 1 meter and 4.82 meters downstream from the driver/driven intersection. These two pressure traces allow us to compare the shocks at those specific locations as the driver length is varied. Additionally, the evolution of the shock between these two locations can be compared.

Figure 2.4 shows that longer drivers can result in the formation of a flat-top wave. Some driven length is needed before the pressure signature generated by the shock tube with a 0.4572 meter driver is representative of a Friedlander wave. However, the overpressures generated 4.82 meters downstream by this shock tube are significantly higher than those generated by shock tubes with smaller driver lengths. Additionally, the positive phase duration is also longer, which would result in greater impulses on the test article.

Figure 2.5 shows the evolution of the primary shock as it travels down the shock tube for a 0.4572 meter driver. At 1 meter downstream from the driver/driven intersection, there is clearly a flat-top wave. The position history shows that the shock strength quickly dissipates between the 1.53 and 2.99 meter locations, but the wave is now more representative of a Friedlander wave by the 2.99 meter location. By the time the shock is 4.82 meters downstream, the resulting pressure signature is once again no longer representative of a Friedlander wave. This study shows that there is a critical area in which the test article should be placed such that the impacting wave exhibits the desired blast profile.

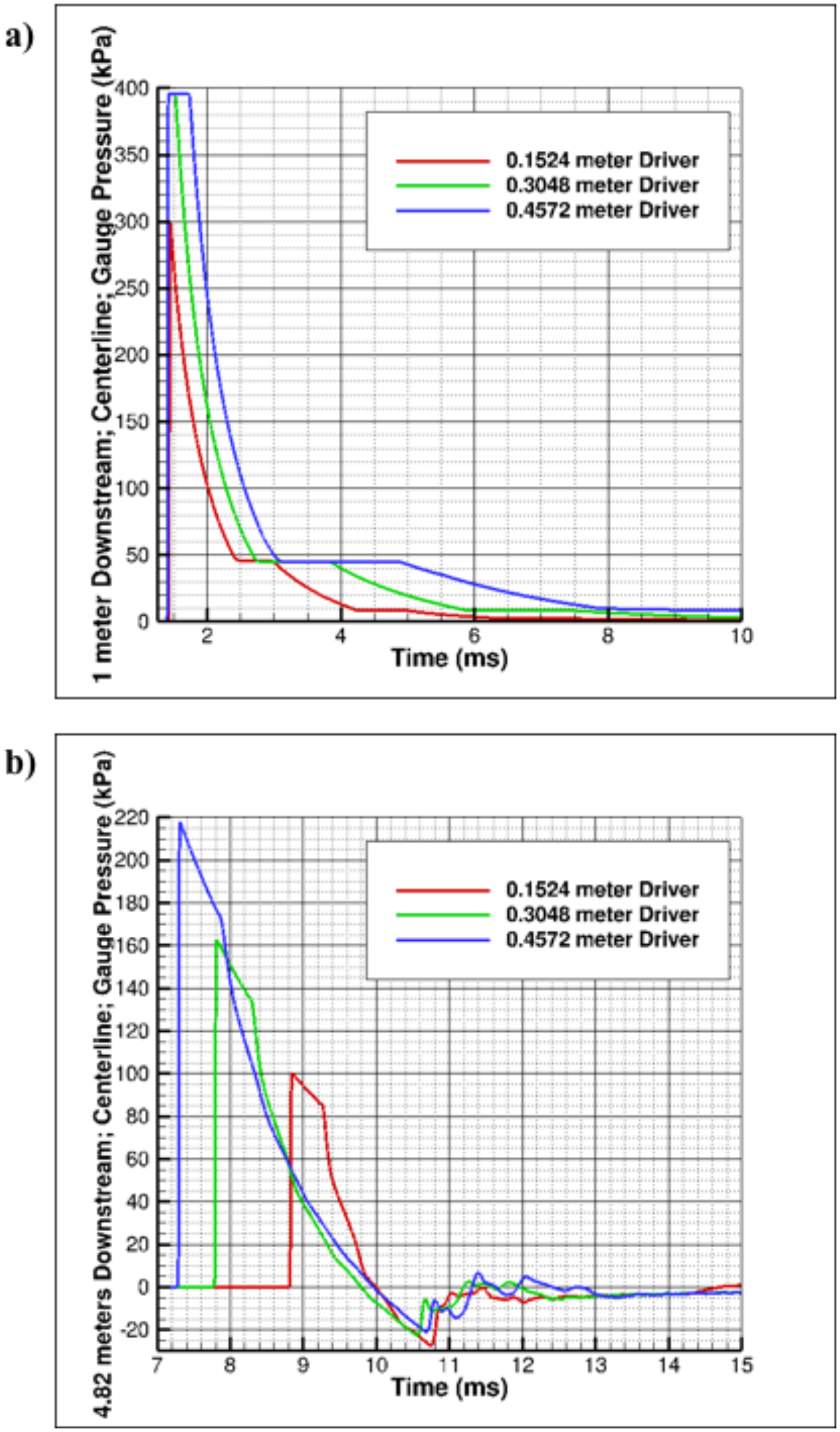

Figure 2.4: Driver Length Study; (a) 1 meter (b) 4.82 meters downstream of driver/driven intersection

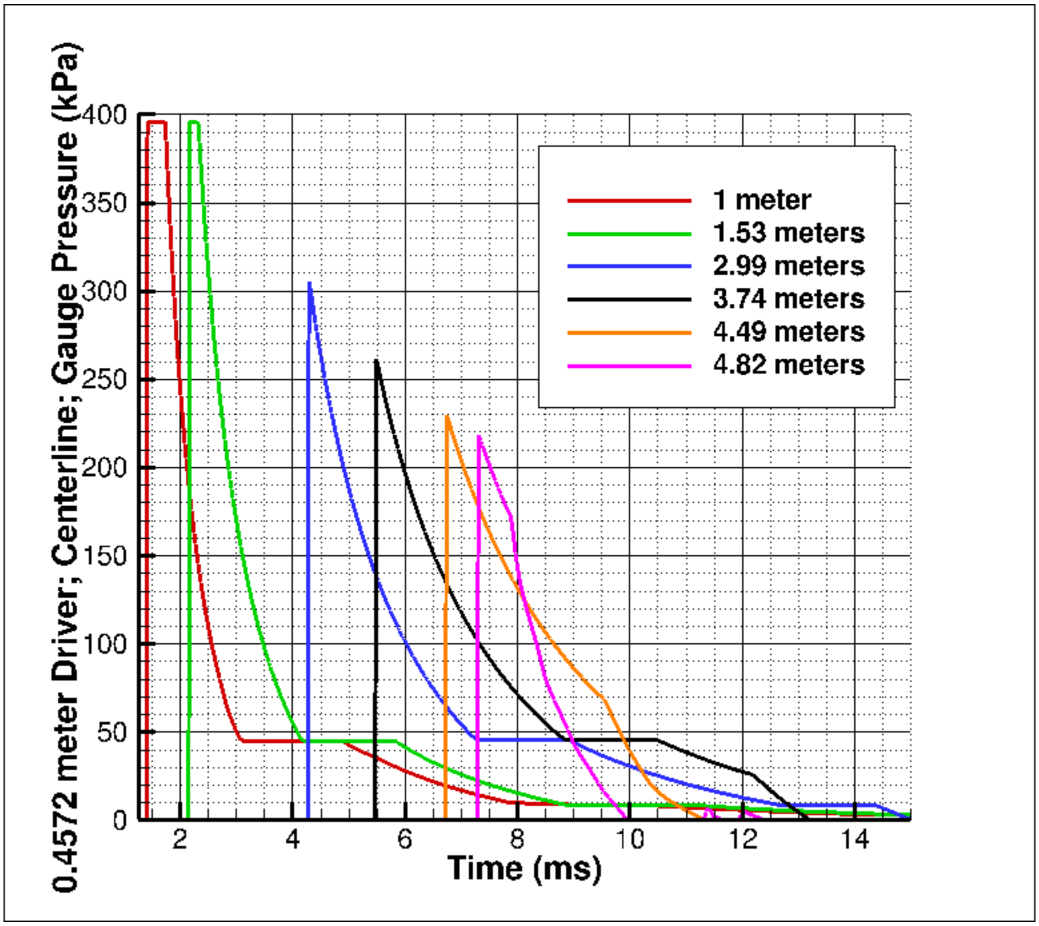

Figure 2.5: 0.4572 meter driver section shock tube shock evaluation

2.4.3. Driver Gas Study

The final study conducted as part of this work was to look at the effect of using air, helium, or an equal parts mixture as the driver gas. The driver gas is an important facet of the experimental setup because IEDs and explosives may release other gases, which may alter the shock properties. In a laboratory setting, it may be less desirable to use explosive nitroanimes, including RDX, due to licensing requirements and the need for specialized equipment for storage and transport [10]. Because one objective of this work is to help inform future experiments, air, helium, and an equal-parts mixture, all of which are more likely to be experimentally used, were studied for this analysis. Pressure traces were compared for each simulation at two separate probe locations: 1 meter and 4.82 meters downstream from the driver/driven intersection. These pressure traces also show how the generated shock profile changes, how the shock evolution/decay changes, and how characteristics such as peak pressure and positive-phase duration are altered.

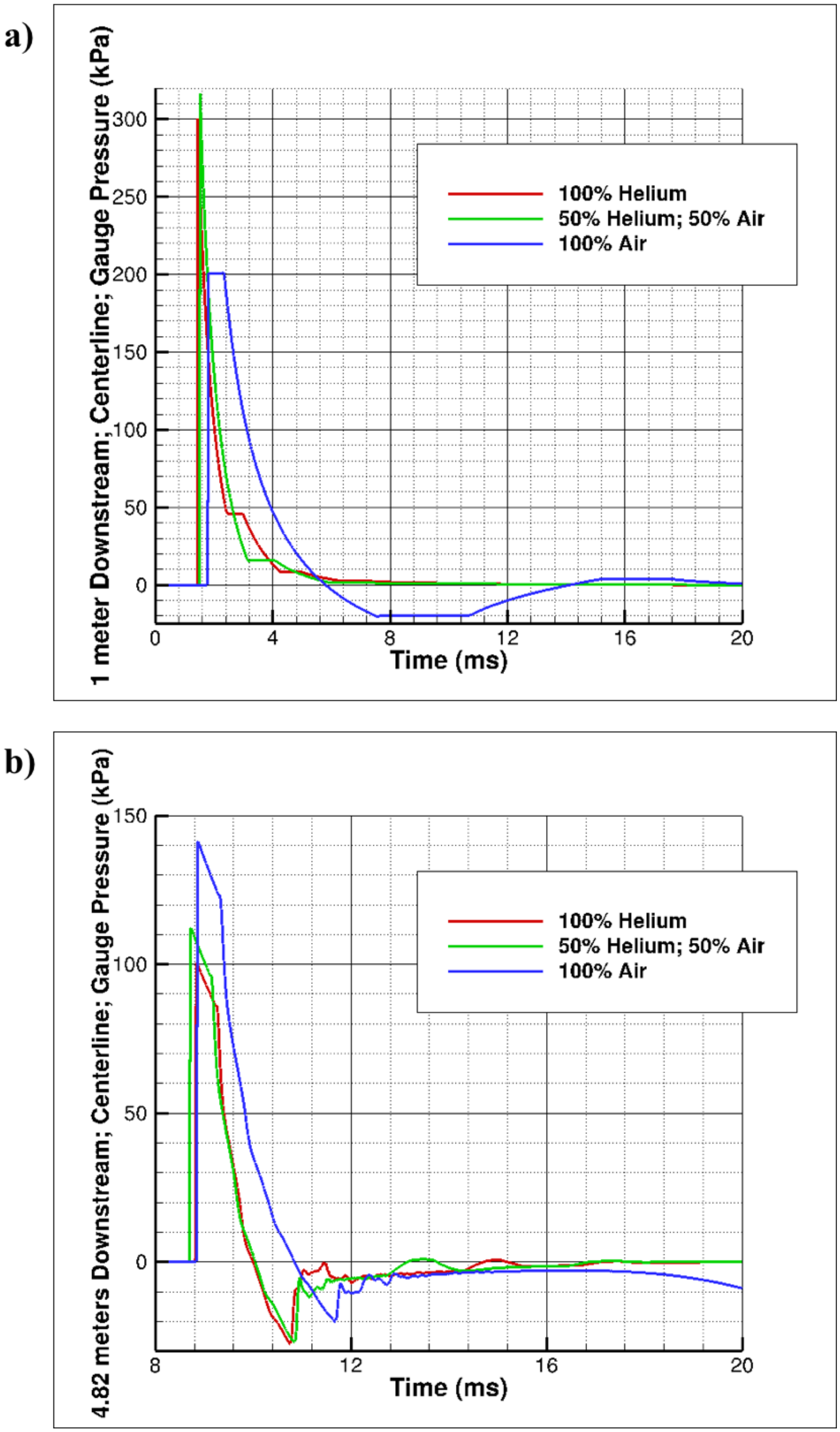

Figure 2.6: Driver gas study; (a) 1 meter and (b) 4.82 meters downstream of driver/driven intersection

From Figure 2.6a, the simulations show that the shock arrival time is the earliest for a helium driver gas and the latest for an air driver gas. This is unsurprising considering that the molecular weight of helium is less than air and it also corresponds to the strength of the shock. Figure 2.6b shows that the order in which the shocks arrive changes such that the shock from a mixture arrives first and the shocks from the air and helium driver gases arrive nearly at the same time. This can be attributed to changes in the shock strength. The shock due to the air driver gas remains the strongest and thus the fastest, enabling that shock to “catch-up” to the other shocks. While both the helium and air-helium mixture produce shock profiles similar to the Friedlander profile, the air driver gas creates a flat-top profile instead.

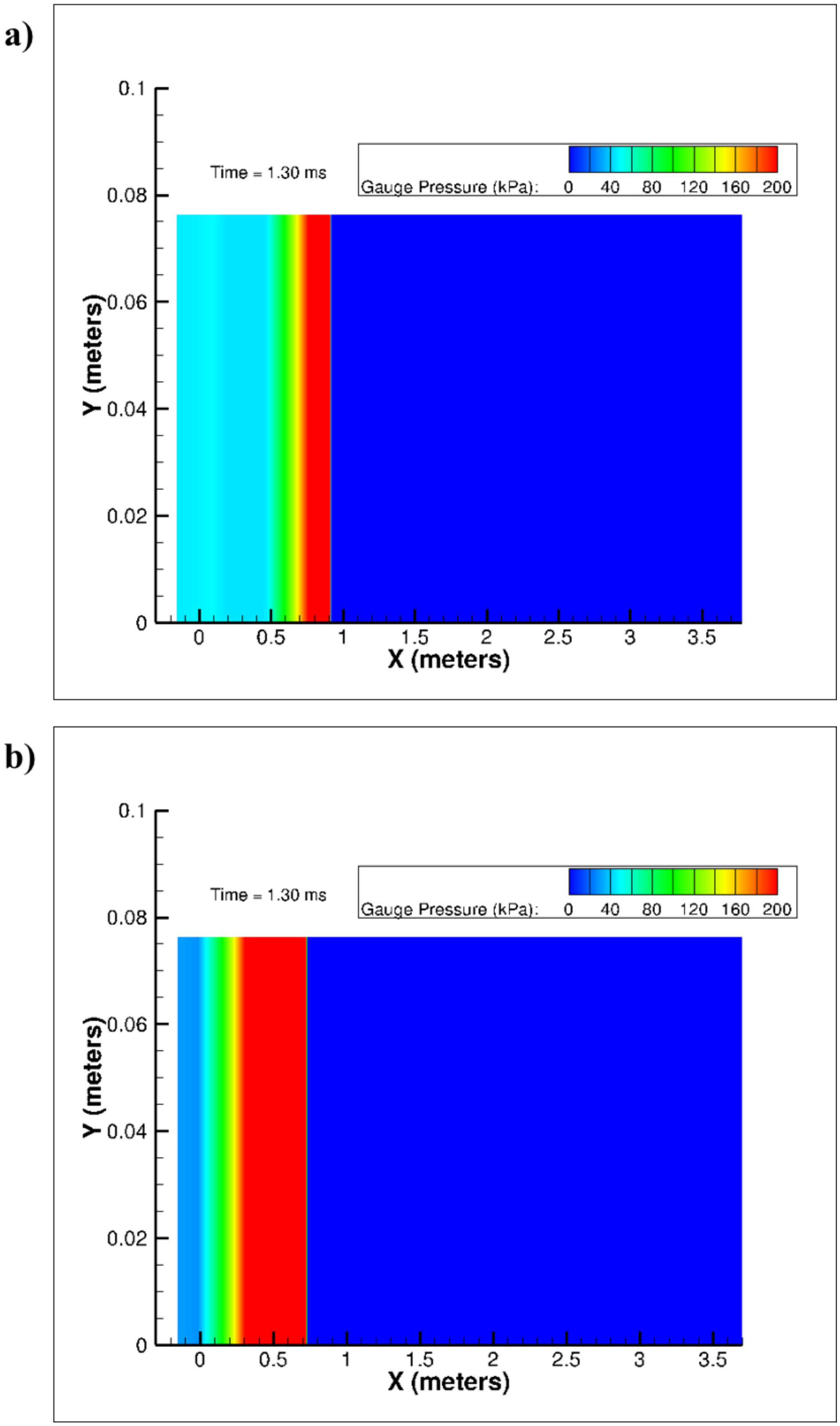

Figure 2.7: Pressure flow contours for (a) Helium driving gas (b) Air driving gas

Figure 2.7a shows a pressure contour for the helium simulation, and Figure 2.7b shows a pressure contour for the air simulation. These flow contours corroborate the pressure signatures observed: the shock for the helium simulation has travelled farther and the thickness of the highest-pressure level is smaller corresponding to the immediate decay in the pressure signature, whereas the air simulation has a thicker region of high pressure which corresponds to the flat-top wave.

If the test section is far away from the start of the driver section, then the results in Figure 2.6b may be more important. From this plot, one can see that the simulations for each gas resulted in similarly shaped pressure signatures sufficiently downstream of the driver/driven intersection. Each pressure signature features a short and linear decay between the initial pressure rise and exponential decay, meaning none of them match the desired blast wave profile.

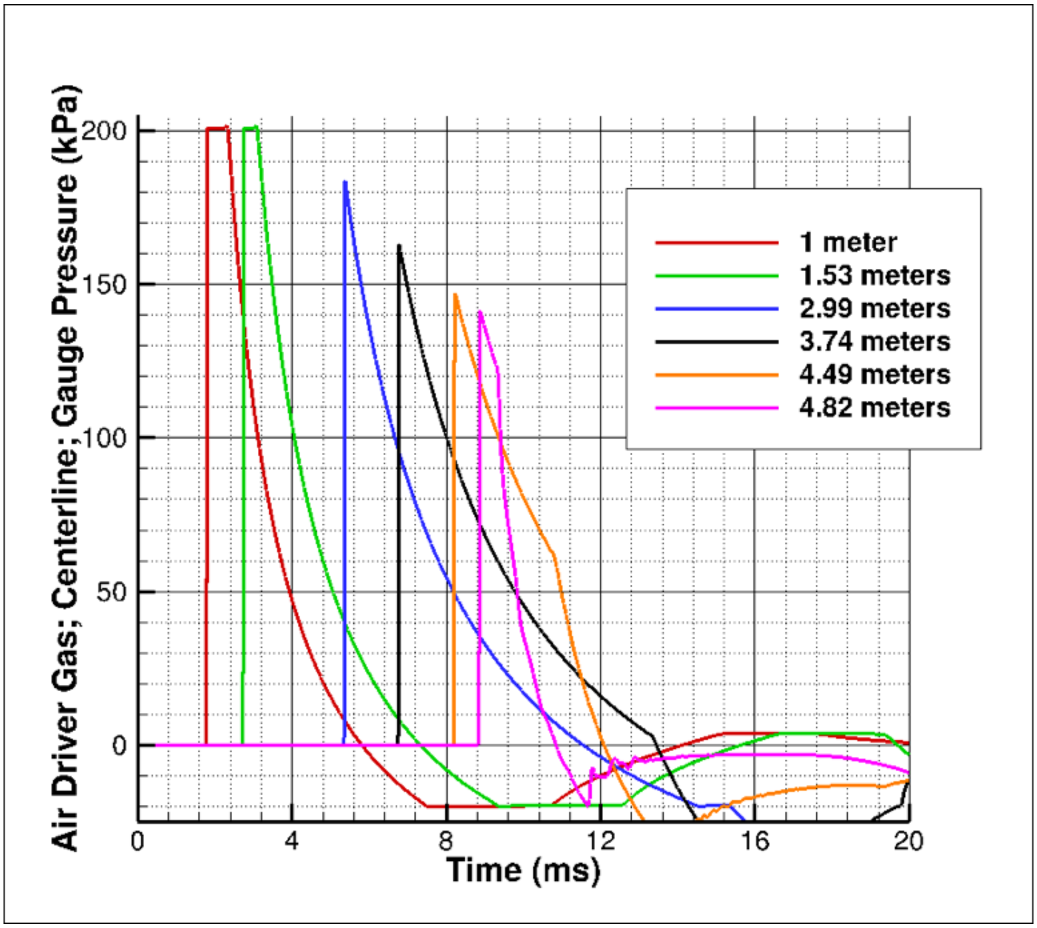

Figure 2.8: Air driving gas shock evolution

Figure 2.8 shows that the blast profile generated by air can generate the desired profile, but it occurs farther downstream than the point where the desired profile is generated when the driver gas is helium. The region in which the desired shock profile is generated is small and, thus, the test section placement would need to be optimized for the conditions of the test. If helium or a mixture are used instead, researchers would likely have more freedom in test section placement. However, both the helium and air-helium mixture show a significant decrease in max pressure with distance relative to the air mixture.

2.5. Discussion

The purpose of this chapter was to provide design guidelines for shock tubes such that they can be used to generate blast waves. Parametric studies were conducted using CFD to characterize the primary overpressure blast environment created by a variety of laboratory shock tube designs. CFD was used to characterize changes in the flow that resulted from varying specific design features, such as: burst pressure, driver length, and driver gas. These studies demonstrated that a shock tube can be used to generate the desired Friedlander-shaped blast profile under two conditions. The test section must be placed far enough from the driver/driven interface that there is no flat-top wave profile. In addition, the test section must be placed far enough from the shock tube exit such that the complex flow phenomena near the shock tube exit do not influence the blast profile. The exact distances that the test section should be placed away from the driver/driven interface and shock tube exit depend on other design parameters such as shock tube length and driving gas.

Experimentalists using shock tubes for this work will have two major goals – to generate both a Friedlander-shaped blast profile and a sufficiently high peak pressure in the test section to correlate the results of free-field testing for a corresponding amount of explosive. The studies showed that the use of air as the driver gas results in a flat-top blast profile that briefly changes into a Friedlander-shaped blast profile farther downstream. The differences in the peak pressure and impulses between flat-top and Friedlander-shaped blast profiles would depend on the exact wave and the time duration of the flat-top portion of the profile, but these differences could lead to incorrect assessments about how injuries occur in the field. Selecting helium as the driver gas immediately results in a Friedlander-shaped blast profile. This is desirable if the test section can be placed close to the driver/driven interface. If the test section has to be placed farther away for other requirements, the use of helium may be detrimental to peak pressure requirements because helium has a higher rate of decay in peak pressure as the wave travels downstream than air. An optimized air-helium mixture for the driver gas may provide both a Friedlander shock profile and required peak pressures in the test section. Experimentalists may be able to meet peak pressure requirements with helium as the driver gas by selecting a diaphragm material that will not burst until higher pressures. As the pressure in the driver section increases prior to burst, the resulting peak pressures in the driven section will also increase. If this option is utilized, the sublinear relationship between burst pressure and the resultant peak pressure of the wave is important to keep in mind.

A key finding of the driver length study was that an increase in driver length can lead to a flat-top wave profile farther downstream the shock tube, even with a helium driving gas. Thus, the test section should be placed sufficiently far away to ensure that the test article is impacted by a shock exhibiting the appropriate pressure decay. The placement of the test section is further complicated by the change in the pressure signature, deviating from the Friedlander profile, as the shock travels downstream. Pre-test predictions using CFD may be used to determine the ideal location for the placement of a test article such that it is impacted by a shock that also provides the desired blast profile and peak pressure. Each study showed that the peak pressure of the shock decreased as it traveled downstream. These two results should drive an experimentalist to minimize the driver length such that the acoustic waves can quickly coalesce and form the strong shock before losses reduce the peak pressure below the requirement for a given test.

In conclusion, the studies demonstrated that shock tubes are a viable method of generating Friedlander-shaped blast profiles. However, careful attention must be paid to the shock tube and experimental design to ensure this profile is achieved while meeting minimum peak pressure requirements in a test section. CFD can be used to help design the shock tube and provide pre-test predictions to verify that all requirements will be met.

3. Assessment of Helmet Effectiveness against Blast Waves using Computational Fluid Dynamics Simulations of Gas-Driven Shock Tubes

3.1. Introduction

The primary objective of the work described here was to use computational fluid dynamics (CFD) simulations, validated against experimental data from laboratory testing, to perform a comprehensive study of shock tube flow and its impact on a head form inside the test section. Simulations were conducted to compare the overpressures experienced by bare and helmeted head forms in front, side, and rear orientations. The author hopes that these results will be used to inform future helmet design for blast wave protection.

3.2. Methodology

The shock tube in this study consists of a high-pressure region (the driver section), separated by a diaphragm from a low-pressure region (the driven section). The diaphragm is made of multiple sheets of acetate and polyester screen material. The sheets of acetate vary in thickness depending on the desired burst pressure and the polyester is used to reinforce the acetate. Depending on the application, the driver section is at a different temperature and is filled with a different gas than the driven section. Once the driver section is sufficiently pressurized causing the diaphragm to rupture, a normal shock travels into the driven section, and an expansion wave travels into the driver section. Researchers at JHU/APL built a shock tube—the Blast Overpressure Simulator System (BOSS)—with a 0.9144m x 0.9144m cross-sectional test-section area. This shock tube was based on a design specifically made to generate pressure signatures similar to those produced by blast waves [18]. Additional information on this shock tube was provided in 1.1.5. The shock tube geometry was modeled using CFD meshing software and the three-dimensional (3-D) unsteady, and compressible equations were solved using CFD software. Additional details on the solver are provided in Section 3.2.2. CFD simulations were conducted for models with unobstructed shock tube conditions, as well as models of a bare or helmeted head form inside the test section.

3.2.1. Baseline Mesh Description

The BOSS was used as the nominal geometry for this computational effort. A 2D schematic of a top-down view of the shock tube is shown in Figure 3.1.

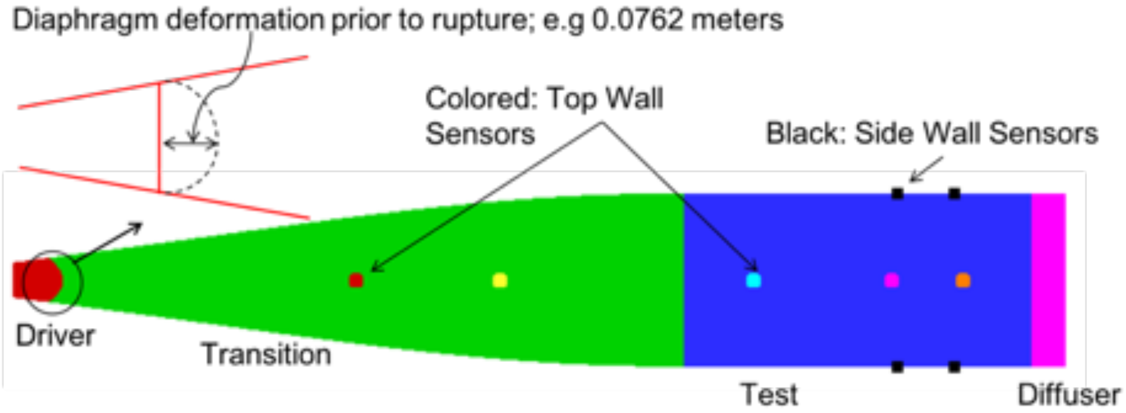

Figure 3.1: Two-dimensional schematic of Blast Overpressure Simulator System

As shown in Figure 3.1, the End-Wave Eliminator was not modeled to reduce the complexity of the mesh. Instead, the mesh's axial spacing was rapidly increased after the test section to artificially diffuse the shock and prevent a reflection off the rear wall of the shock tube from influencing the test section. The diffusor section behind the test section is longer than what is depicted in the figure. Experimental pressure sensors along the top wall are depicted by colored cubes, while sensors along the side walls are depicted by black cubes.

Although it is easier to model an instantaneous and complete diaphragm rupture, non-metal diaphragms may deform prior to rupture and may not fully rupture. Active research on this topic includes both the numerical analysis of non-ideal diaphragm rupture in expansion tubes [24] and experimentation with instantaneous diaphragm rupture techniques such as laser beam irradiation [24, 25]. An image of a diaphragm that both bulged and failed to rupture during testing at the JHU/APL BOSS facility is shown in Figure 3.2. Diaphragm deformation prior to rupture was modeled through spherical deformation of the driver section where the radius could be changed to model different levels of bulging. A small computational study was conducted to determine what bulging levels in the CFD model led to results that best matched experimental data.

Figure 3.2: Failed diaphragm

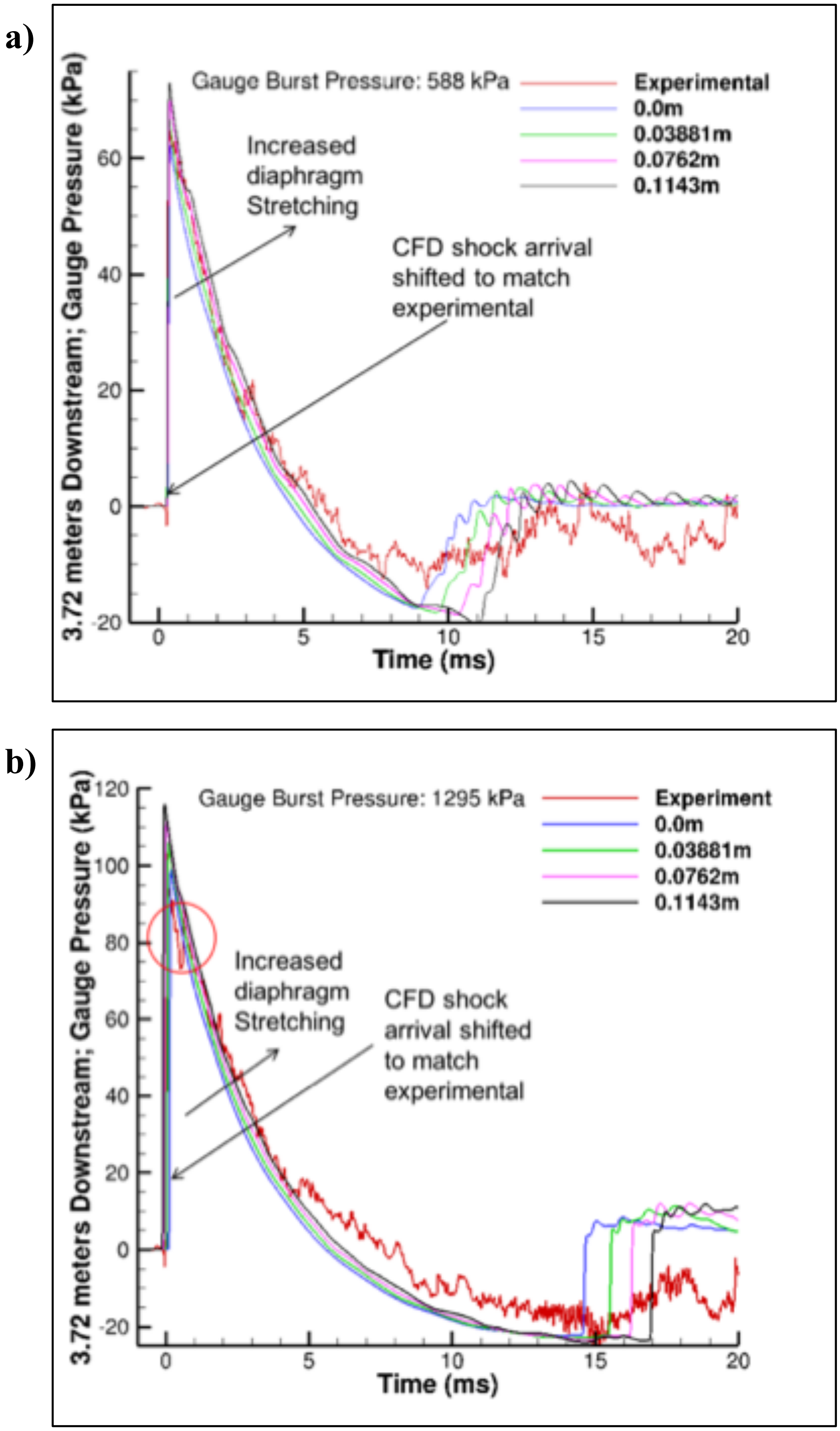

Figure 3.3: Diaphragm deformation study for (a) 588 kPa (b) 1295 kPa burst Pressure

Figure 3.3 shows the comparison of experimental runs to computational simulation results for various levels of deformation modeled. The burst pressures in the CFD simulations were set to match the burst pressures for the corresponding experimental runs. The plots suggest that 0.0762 meters of deformation results in a pressure trace that best matches the experimental data. It is also worth noting that there is secondary spike in the experimental data that was taken at a gauge burst pressure of 1295 kPa. It is believed that the secondary spike was caused by an acoustic wave that coalesced with the primary shock front later than expected due to non-ideal diaphragm rupture. Although the peak pressure is lower than the predicted peak pressure for a 0.0762 meter deformation, the two curves show good agreement after the secondary spike in the experimental data. Furthermore, due to the simplicity of the model and variability in the experiment, an exact match was not expected.

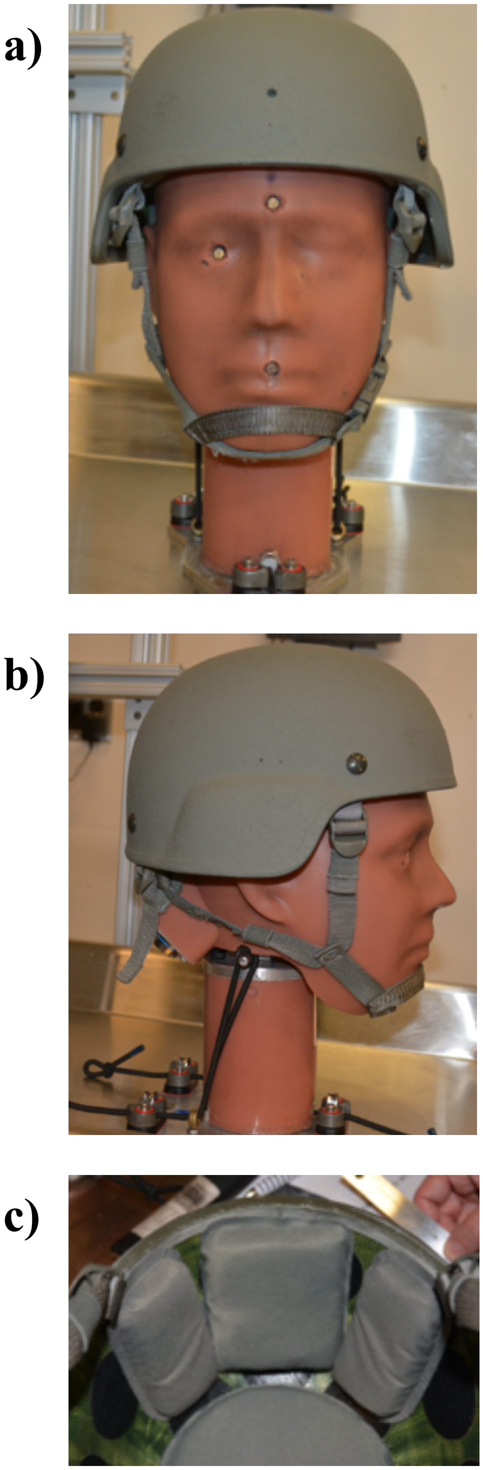

Figure 3.4: Helmeted head from (a) front view (b) side view (c) helmet padding underside view

Figure 3.4 shows images of the head form and helmet geometries that were modeled for this study. The underside of the helmet is also shown, with some of the padding that makes contact with the head.

A hybrid meshing technique was employed to increase the flexibility of the mesh. GridPro[5], an automatic multiblock structured grid generation tool, was used to create a fully structured grid of the shock tube interior with a spherical cut-out in the test section, as shown in Figure 3.5. This figure also depicts the stretching of the grid spacing used to dissipate the shock after the test section in the simulations.

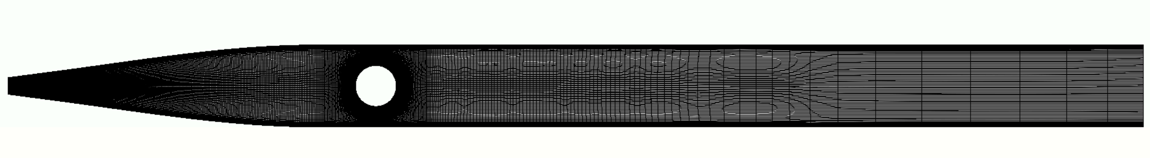

Figure 3.5: Two-dimensional slice of GridPro-generated computational mesh of shock tube with spherical cut out in test section

Figure 3.6 shows a zoomed in view of the mesh near the driver/driven interface and the curved grid lines that model diaphragm deformation.

---

[5] The software GridPro and more information about it and about Program Development Company can be found at http://www.gridpro.com/

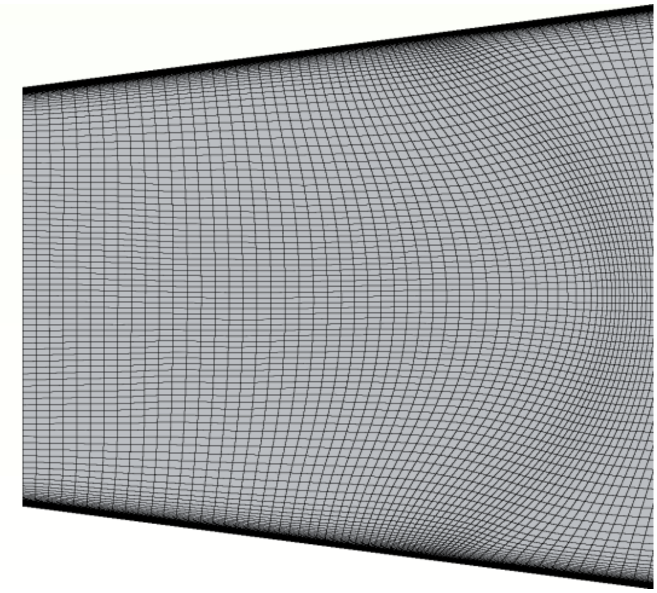

Figure 3.6: Zoomed-in view of two-dimensional slice near driver/driven interface (curved grid lines model deformed diaphragm)

Figure 3.7 shows a zoomed in view of the 2D slice and spherical cut out in the structured GridPro mesh. The boundary of this cut out was extracted from GridPro, brought into Pointwise[6], and used as the outer boundary for the mesh around the test article.

---

[6] The software Pointwise and more information about it is available at www.pointwise.com

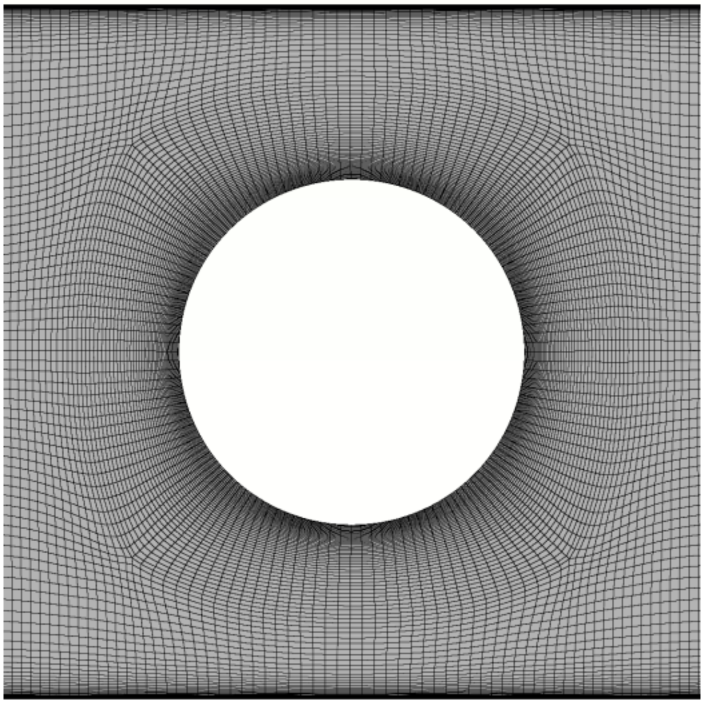

Figure 3.7: Zoomed-in view of two-dimensional slice showing spherical cut out

Pointwise can be used to create structured, unstructured, overset, and hybrid meshes. For this study, Pointwise was used to create an unstructured grid between the test article geometry and the aforementioned spherical outer boundary. Pointwise's T-Rex feature, which utilizes anisotropic tetrahedral extrusion to create hexahedra off walls and tetrahedral cells farther away, was used to generate the mesh around the test articles. Figure 3.8 shows the boundaries for one of the generated grids, where the test article was a helmeted head form.

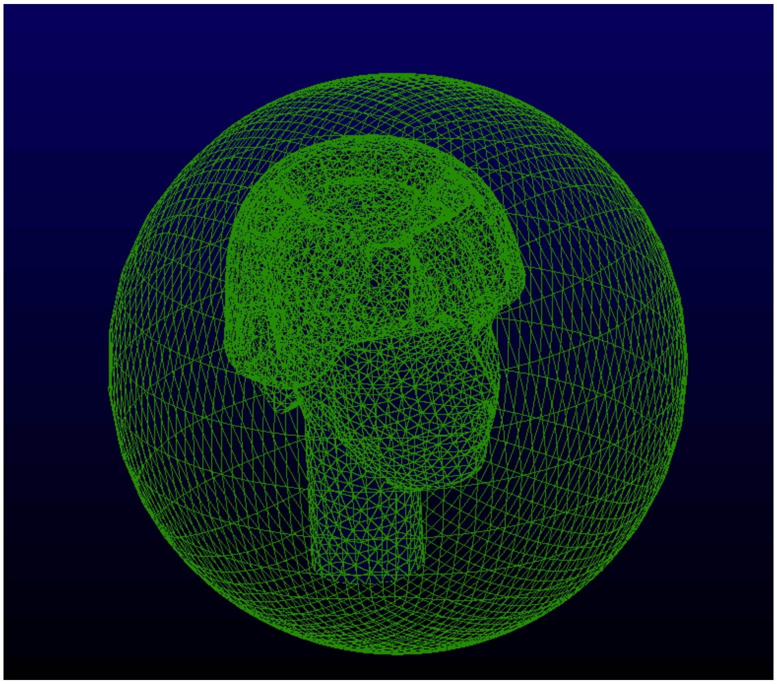

Figure 3.8: Isometric view of spherical boundary shared between both meshes and Pointwise-meshed head-helmet geometry

This approach allowed for the test article to be swappable (i.e., only the unstructured Pointwise mesh would need to be regenerated to conduct simulations with different test articles), while keeping the spherical boundary the same. Additionally, the spherical mesh could be rotated to study the impact of test article orientation with respect to the incoming shock wave, while maintaining point-to-point connectivity at the spherical boundary. The two separate meshes were then combined in Pointwise, as shown in the zoomed in view in Figure 3.9.

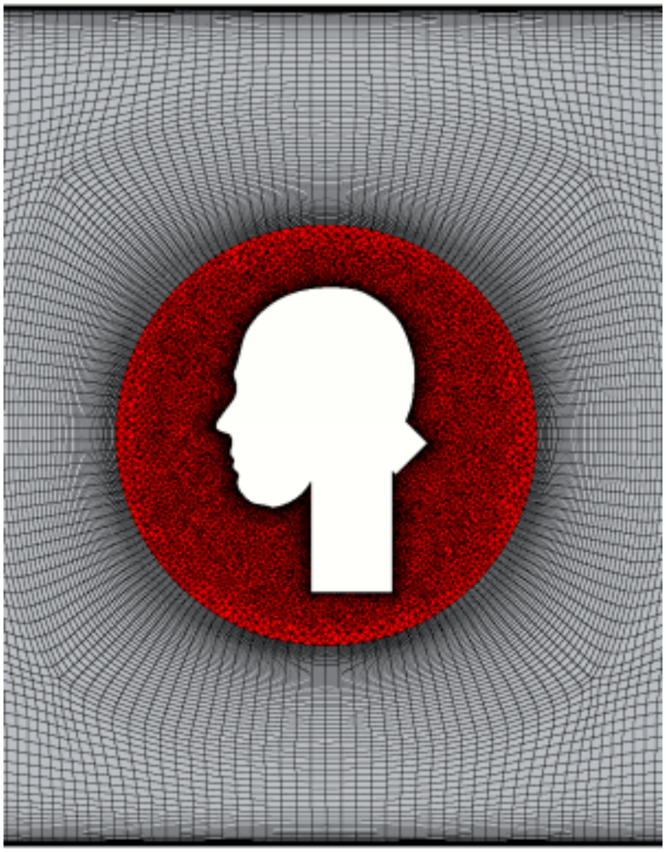

Figure 3.9: Zoomed-in two-dimensional slice of merged mesh with GridPro-generated shock tube mesh and Pointwise-generated mesh around test article

3.2.2. CFD Solver and Settings

CFD++ (version 15.1.1.u6), a commercial CFD solver developed by Metacomp Technologies Incorporated, was used for all the simulations described in the following studies. CFD++ is a versatile and generalized code that can solve the one, two, or three-dimensional, steady or unsteady, incompressible or compressible Reynolds-Averaged Navier Stokes (RANS) equations for viscous flows. The code uses a finite volume formulation, a total variation diminishing scheme for spatial discretization, an implicit time-stepping algorithm for time discretization, and a modified Roe's Riemann solver for updating cell averages in time [20].

For the work described in this report, all simulations were set up to solve the three-dimensional (3-D) unsteady, and compressible equations. For each time-step and grid cell, the code solves the five 3-D conservation equations: mass, x-momentum, y-momentum, z-momentum, and energy. Two additional equations are solved for the realizable k-ε turbulence model, which is recommended by Metacomp Technologies Incorporated for internal flows. A turbulence model study (not shown for brevity) found insignificant differences between the pressure signatures generated from simulations with different turbulence models, but did find that including some turbulence changed the resulting solution.

When solving flows that involve multiple species, an additional N-1 equations are required, where N is the number of species. For this work, pressurized air was modeled in the driver section to match the experimental set up. Since only one gas species was modeled for the entire simulation, no additional equations needed to be modeled. It should be noted that Reener et al. found significant differences in the pressure signatures based on the driver gas [10]. Not only did Reneer et al. find that different driver gases affected the pressure signature's match with the Friedlander wave, but they also found that the injury to the brain differed significantly for different driver gases [10].

The flow through a shock tube is fundamentally unsteady. The implicit (backward Euler), dual time-stepping algorithm was used to advance the solution from one physical time-step to another. At each global iteration (or time-step) the dual time-stepping algorithm iteratively solves the governing equations for some pre-defined number of inner iterations or until a predefined convergence is satisfied. In simulating unsteady flows, the selection of the physical time-step is critical and is highly dependent on the velocities in the flow and the size of the smallest grid cell. If the time-step is chosen to be too high, the flow solution is unphysical and could become unstable. If the chosen time-step is too low, then the overall simulation (wall-clock) time can become very large. These issues are exacerbated when dealing with complex flows because of the need to have large grids. For this work, the time-step was set to 1 microsecond, based on time-step independence study.

Mesh resolution was based on a mesh independence study to ensure adequate accuracy of the shock propagation. Both of these results were important because an under-resolved mesh would create artificial dissipation of the shock, while a time-step that is too large could make reduce the stability of the simulations leading to spurious oscillations, particularly near discontinuities such as shocks (Gibbs phenomena) [21, 22, 23]. Most cases were run to achieve at least 15 milliseconds of flow time. The maximum number of inner iterations was set to 30 to achieve a convergence of two orders of magnitude. Early in the simulations, the code required 15 to 30 inner iterations to reach convergence. When the shock arrived near the test article and the flow became more transient again, 15 to 30 inner iterations were required to reach convergence. However, for the majority of the simulation where the problem was a simple 1-D propagation of the shock, only 6 to 8 inner iterations were required for convergence.

3.2.3. Initial and Boundary Conditions

Each CFD simulation requires initial conditions (ICs) and boundary conditions (BCs). Here, the driver section was initialized with the driver gas at a given gauge burst pressure of 1295.85 kPa. The remaining ICs are shown in Table 2.

Table 2 Initial Conditions

Region	**Absolute Pressure (Pa)**	**Temperature (Kelvin)**	**XYZ Velocity (m/s)**
Driver	Burst Pressure	295	(0,0,0)
Driven	101325	295	(0,0,0)
Farfield	101325	295	(0,0,0)

At all solid surfaces (shock tube walls, head form, and helmet), boundaries were modeled as adiabatic walls.

3.2.4. Data Analysis and Post-processing

The focus of this work was to study the interaction between a blast wave and bare and helmeted head forms in different orientations. Several points along the shock tube top and side walls were probed. These locations corresponded with pressure sensor locations on the JHU/APL shock tube, which are depicted in the 2D schematic shown in Figure 3.1. Similarly, specific points corresponding to experimental sensor locations were probed for both the bare and helmeted head forms. The locations of these probes are shown in Figure 3.10. The X, Y, Z coordinates of each probe location were provided to the CFD code and the corresponding pressures at each time-step were recorded to a file as the simulations were running. The data was recorded at every time-step. Additionally, the flow-field contours of a slice along the centerline were saved every 25 time-steps.

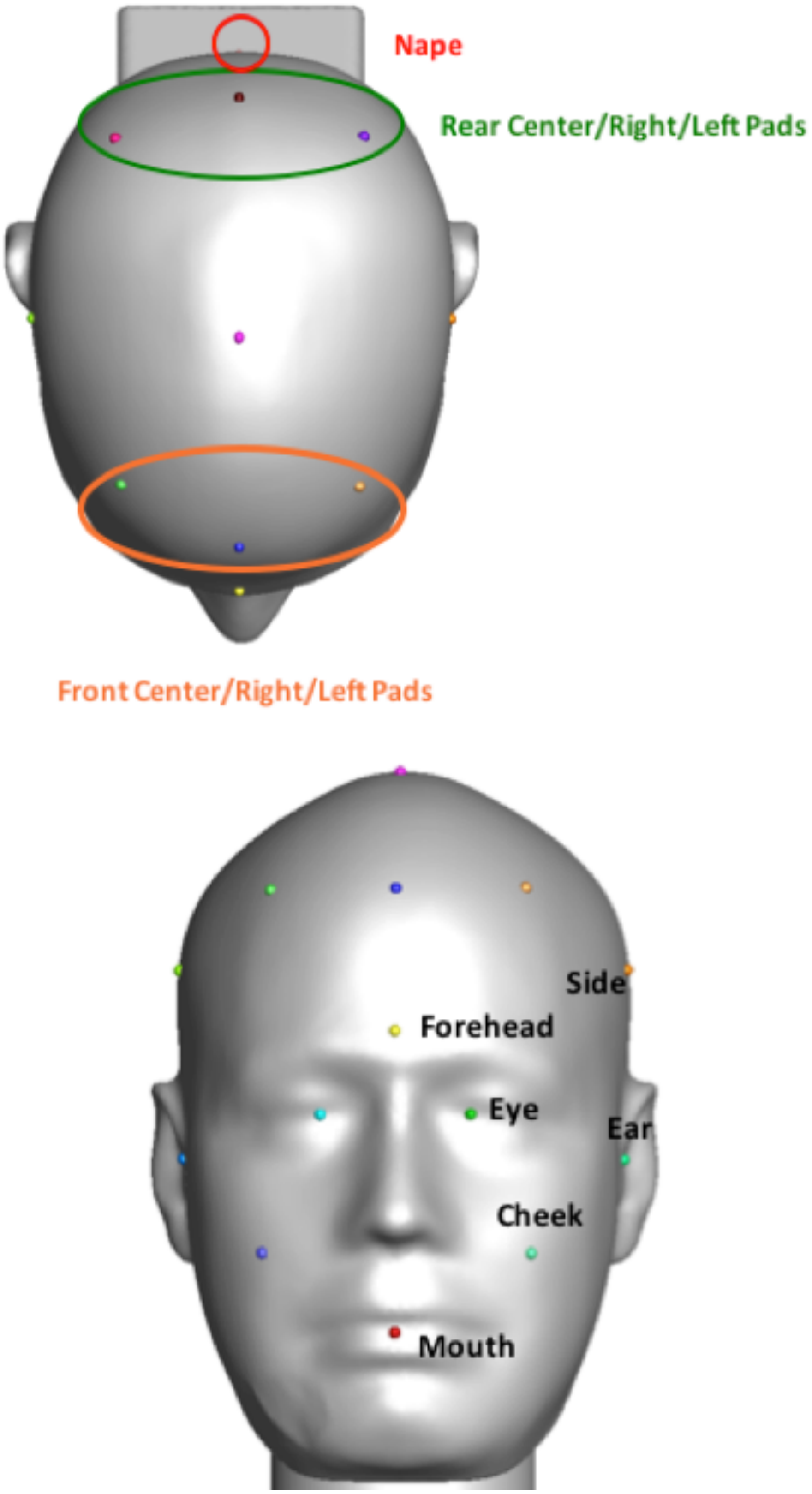

Figure 3.10: CFD probe location and experimental sensor placement on bare head form

3.2.5. CFD Model Assumptions

CFD modeling assumptions related to diaphragm deformation and modeling of an idealized membrane rupture were discussed in Section 3.2.1. Additionally, the CFD model assumes that the test article is composed of rigid, non-moving walls when modeling a test article in the shock tube. In reality, the interface connecting the head forms to the bottom wall of the shock tube is flexible and allows for movement of the head form. It is expected that the motion will likely increase the rate of decay in overpressures, particularly for the forward-facing side of the head.

Although the head and helmet are separate entities in reality and in laboratory experiments, the CFD models them as a single entity. Thus, the helmet's position relative to the head form is fixed and no movement or compression occurs in the CFD simulations. The current CFD model is not able to simulate kinematics and resulting changes in overpressures. Additionally, the pads that make contact with the head form are also modeled as rigid and without any porosity in the CFD model. These modeling assumptions may reduce how quickly pressure underneath the helmet can dissipate and increase the overall pressures and pressure spikes caused by reflection underneath the helmet.

3.3. Results

3.3.1. Shock Formation

A key advantage of using the BOSS is that it ensures the generation of a planar shock front. Therefore, a CFD simulation was conducted with an empty test section to study the shock evolution along the length of the shock tube. Figure 3.11 displays pressure contours as the shock travels downstream the shock tube. At time zero, the region of high pressure is extremely curved due to diaphragm deformation, but the pressure contours clearly depict how the shock straightens out as the wave travels downstream in the test section.

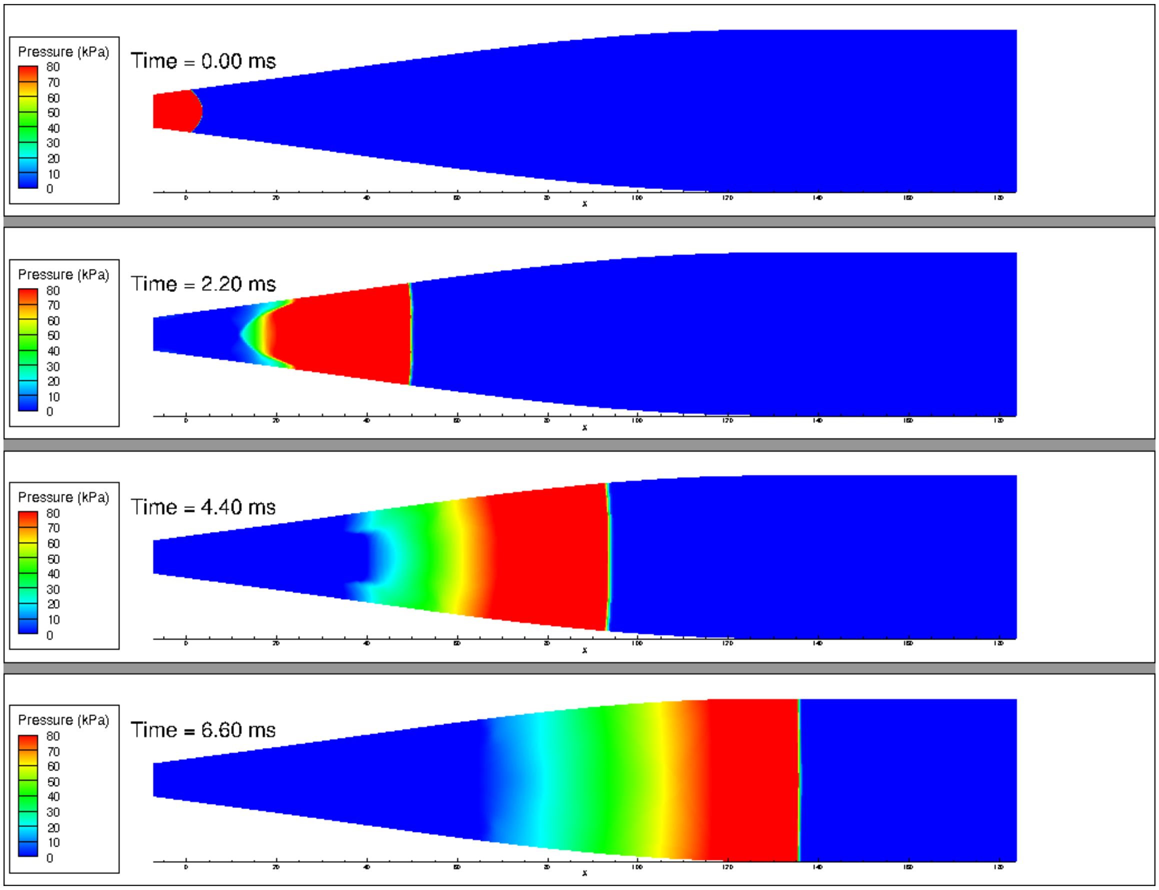

Figure 3.11: Pressure contours and shock evolution

3.3.2. CFD Model Validation

3.3.2.1. Shock Tube Walls

Prior to analyzing the CFD-predicted overpressures on the bare and helmeted head forms, it was important to validate the CFD results relative to the available experimental data. Although the CFD model only has a limited capability to accurately model the diaphragm rupture, it should be able to accurately predict the pressure signature some distance downstream. The CFD and experimental data were first compared 3.147 meters downstream of the driver/driven interface, near the end of the transition section, as shown in Figure 3.12. Both sets of results were shifted in time (x-axis) such that the shock arrival was at time zero. From these results, it is evident that both the experimental peak pressure and positive phase duration predicted by the CFD simulations are within 20% of the experimental results, despite noise in the experimental sensors. Furthermore, the data were once again compared at the start of the test section, 3.72 meters downstream of the driver/driven interface. The same shift in time that was applied to the earlier comparison was applied once again. Both the experimental and CFD results show that the shock travels the 0.576 meter distance between the two sensor locations in about 1.2 milliseconds. Furthermore, the peak pressure predicted by the CFD simulations match the experimental peak pressure at this location within 5% and the positive phase duration prediction is still within 20% of experimental results.

a)

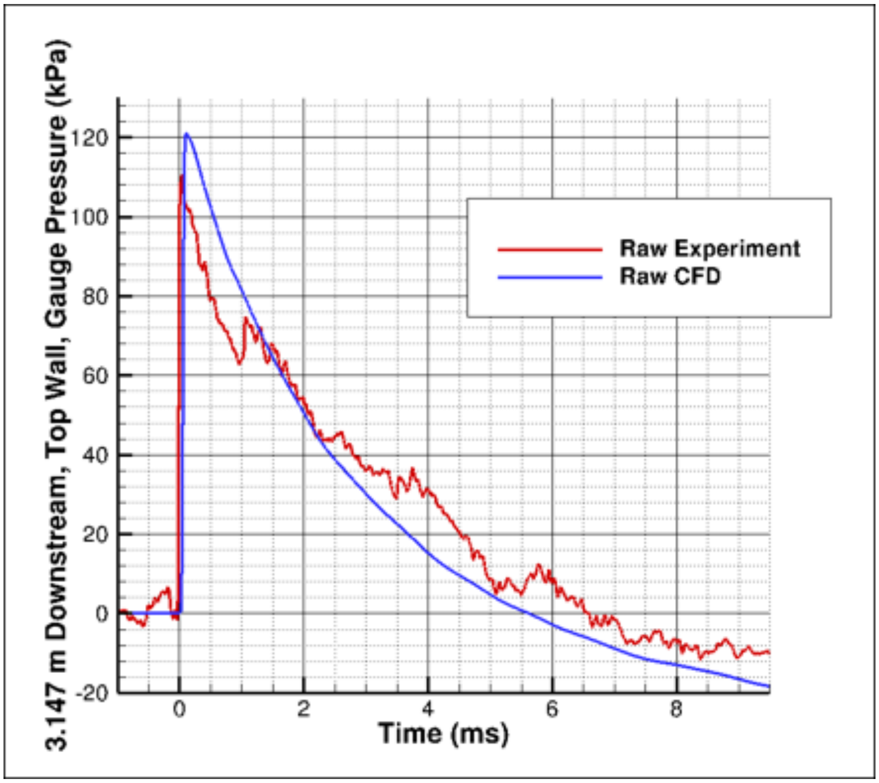

b)

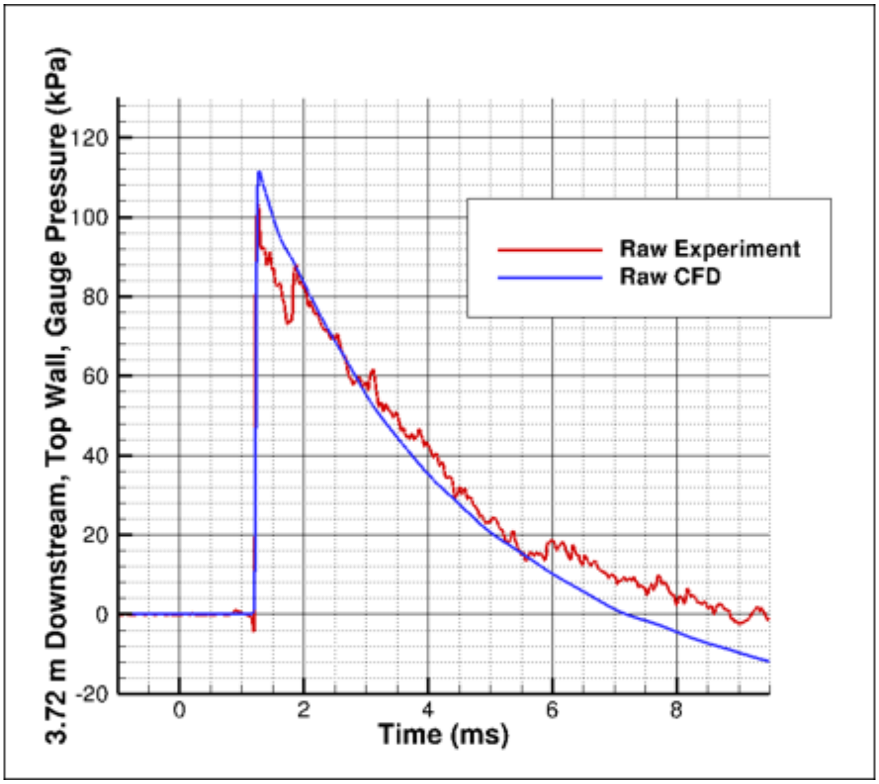

Figure 3.12: CFD validation of pressure time-history for shock tube wall sensors for (a) 3.147m (b) 3.72m downstream of driver/driven interface

3.3.2.2. Bare and Helmeted Head Form

Experimental data for the pressure sensors on the head forms were only available with the head forms oriented to face the oncoming shock. Due to noise in the experimental data and concerns about the filtering process, both raw and filtered experimental data were compared to the CFD results. For brevity, comparisons are shown and analyzed for only the forehead, right eye, and side right sensors.

Figure 3.13 shows the comparison of experimental and computational data for the bare head data. Once again, the CFD predictions for peak pressure continue to be within 20% of the raw experimental data and predictions for the positive phase duration lie within 20% of the filtered experimental data. Furthermore, the computational data shows good agreement with the filtered data traces and mostly lies within the scatter of the raw data. The CFD data consistently predicts both lower peak pressures and lower rates of decay than observed in the experiment. Given the agreement between CFD and experimental data in the flow immediately prior to the test article, it is possible that the peak pressures are being under-predicted due to a lack of sufficient mesh resolution on the head form and immediately near the head form. As mentioned in Section 3.2.5, the CFD model does not simulate any head motion, which is likely contributing to the lower rates of decay in overpressure.

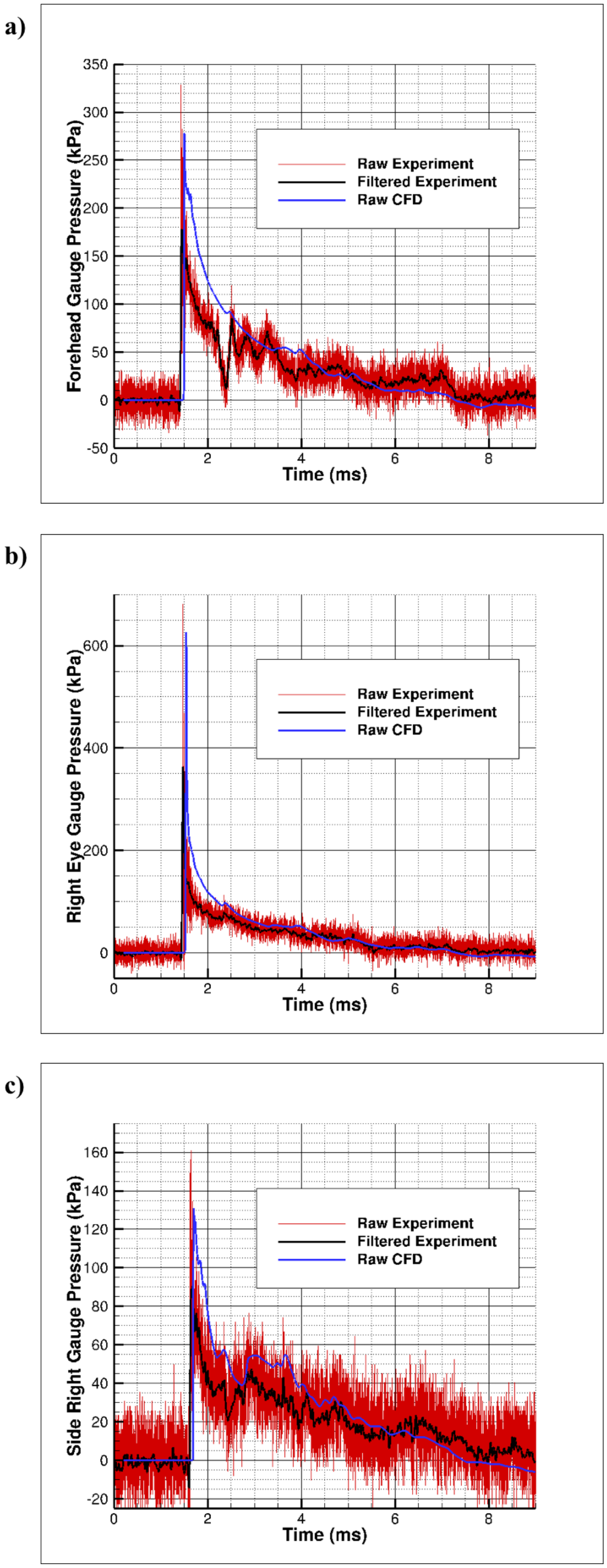

Figure 3.13: CFD validation of pressure-time history for bare head sensors

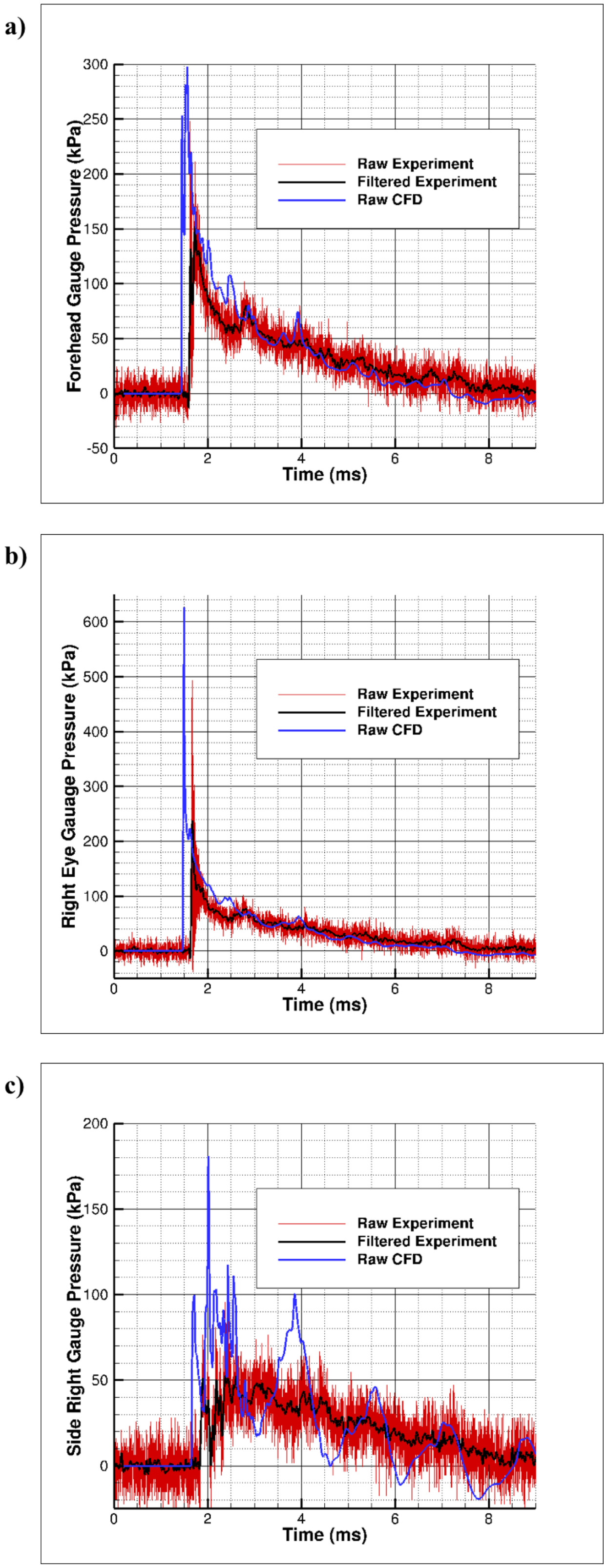

Figure 3.14: CFD validation of pressure-time history for helmeted head sensors

Figure 3.14 shows a similar comparison for the helmeted head data. The majority of the pressure-time history trends show good agreement, suggesting that the CFD models predict these flows well. The shock arrival time and positive-phase time duration are in good agreement between the CFD model and experimental data. However, the agreement between experimental and CFD data is worse than the agreement shown for the bare head form data. The CFD-predicted shock arrival time is slightly earlier than the experimental data suggests and the peak pressure differences are larger. The peak pressure at the side right location is the second local maximum in the CFD data set, which is also captured in the filtered experimental data. However, the magnitude of these pressure peaks is higher in the CFD data. Furthermore, although the trends are different for the side right location as the experimental data shows a constant decay and the CFD shows an oscillating decay, the rate of decay appears to be similar.

3.3.3. Additional CFD Results

Additional results and analyses performed using only CFD results are shown in this section. Experimental data was unavailable for side and rear impact conditions.

3.3.3.1. Frontal Impact

Figure 3.16 shows CFD predictions of the pressure-time history at both previously shown and additional locations around the bare and helmeted head forms for a frontal impact. Unsurprisingly, as the location of the probe moves away from the front of the face, the peak pressure decreases. This is most noticeable at the right ear, side right, and nape locations. The highest peak pressures are observed at the right eye location for both the CFD data shown in Figure 3.16 and experimental data shown in Figure 3.13 and Figure

3.14. This peak pressure observation holds for both the bare and helmeted head form. The same trend was observed in free-field testing by NRL researchers, who showed that a face shield (e.g., goggles) was needed to reduce the overpressures around the eyes [6]. An explanation for why the highest overpressures are observed at the eyes is the natural geometric gradients contained within an average human face. The eye cavity serves as a geometric valley where flow can stagnate, greatly increasing the pressure, as shown in Figure 3.15a. When comparing Figure 3.15a, which shows the geometric gradients on the average male face, with Figure 3.15b, which shows a contour of the maximum pressures observed at any time during the CFD simulation at each discrete mesh point on the face, it is evident that many of the pressure contour lines align fairly well with many of the geometric lines.

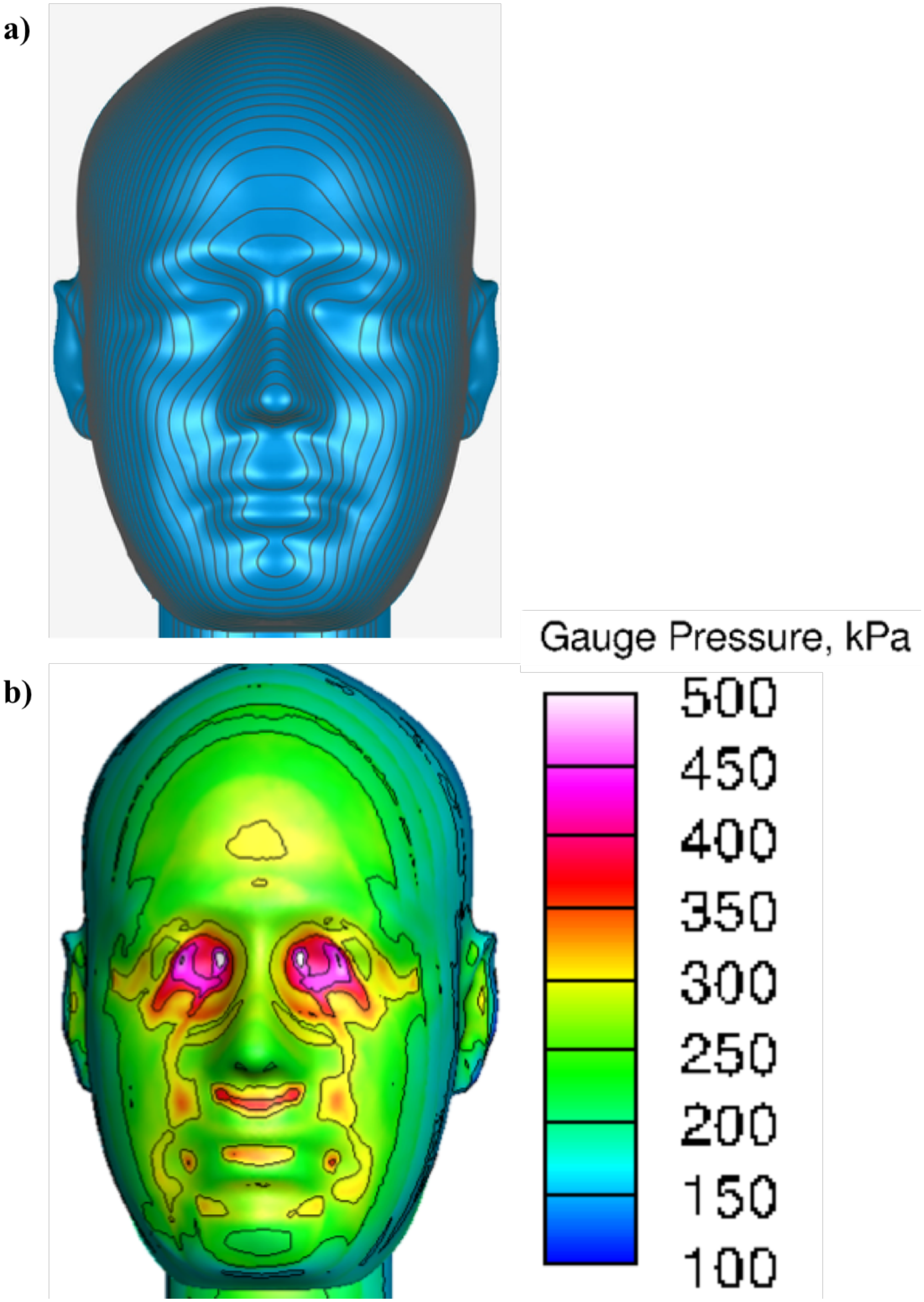

Figure 3.15: (a) Geometric gradients on average male face (b) Maximum overpressure for frontal impact

The lowest peak pressure observed is at the side right location and not the nape. This is likely due to an intersection of waves meeting together at the back of the head form and increasing the overpressures near the nape, which were originally bifurcated at the front of the head form. A second explanation for higher pressures at the nape when the head form is helmeted is the occurrence of reflections from the helmet onto the rear of the head. Similar phenomena were observed by NRL when testing a head form protected by a helmet liner [6].

Figure 3.16 also shows that, for this particular PPE geometry, peak pressures were reduced at the right ear and side right locations. However, although the initial peak pressures were reduced, interactions and reflections under the helmet caused secondary peaks and potentially higher overall impulses. In some cases, such as the location of the nape, the peak pressure actually increases and there are also additional oscillations from reflections under the helmet further increasing the overall impulse. It should be noted that the NRL researchers also observed similar effects; however, the exact locations of these interactions varied due to differences in their PPE geometry [6].

a)

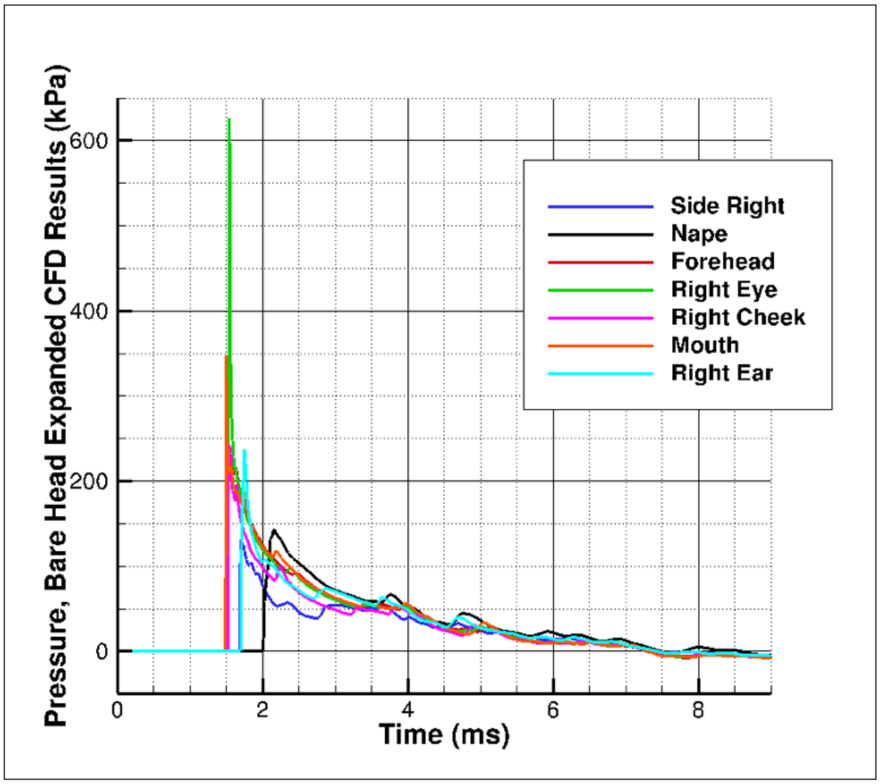

b)

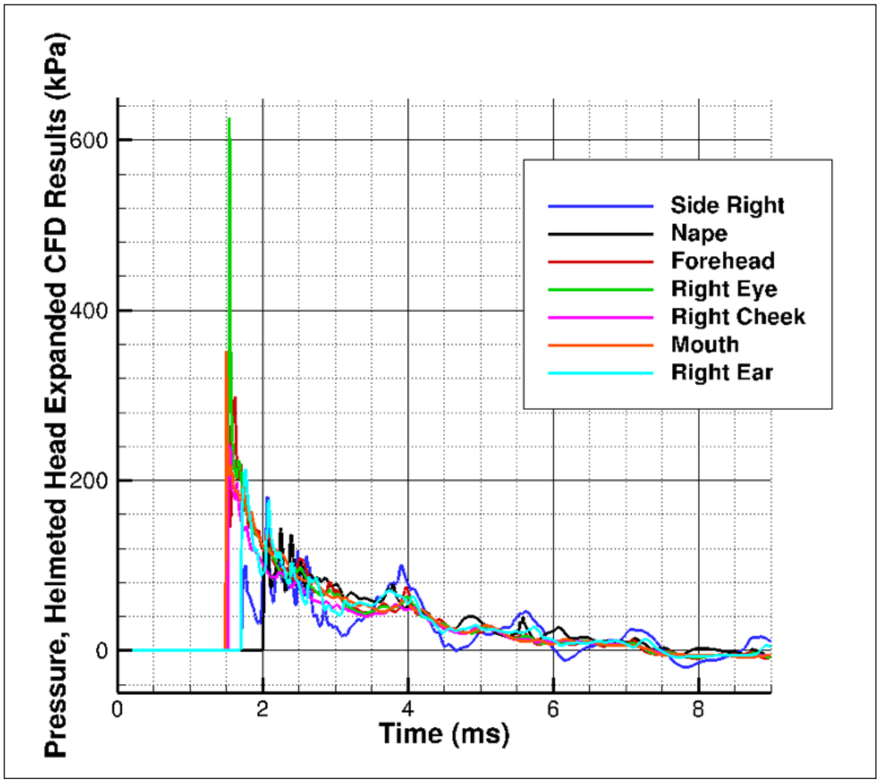

Figure 3.16: Additional CFD pressure time-history results for frontal impact

Figure 3.17 shows the maximum pressure observed at each point along the head and neck surface at any point during the blast wave's impact. It is evident from this image that regardless of the helmet, the eyes still experience the highest pressures. Furthermore, the existence of a helmet creates pressure hotspots in areas where the flow reflects off the helmet's pads and back onto the head.

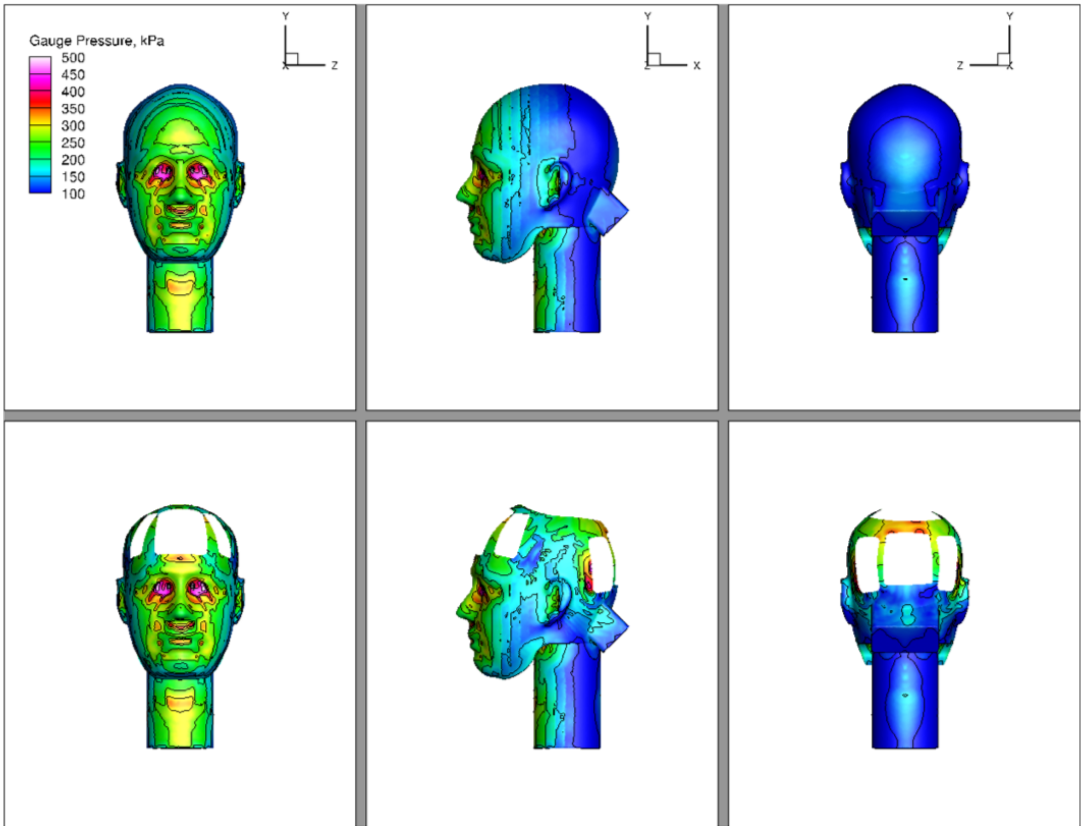

Figure 3.17: Maximum pressures observed for a frontal impact for bare and helmeted head forms

3.3.3.2. Side Impact

Figure 3.18 shows CFD predictions of the pressure-time history at both previously shown and additional locations around the bare and helmeted head forms for a side impact occurring at 90 degrees from a face-on impact. The test article was turned such that the right side of the face was impacted by the shock first and the left side of the face was somewhat protected. There is a significant decrease in peak pressure for both eyes and the forehead relative to the frontal impact scenario. The helmeted head form has lower peak pressures at the right ear location compared to when it is unprotected. The peak pressures at the side left location is higher for a protected head form, which is likely due to reflections between the head and helmet. However, overall pressure magnitudes for locations where the face is exposed are not significantly impacted.

For a protected head form, there are additional oscillations in the data at the side left and side right locations, which are also likely due to reflections. These reflections and secondary pressure peaks will likely increase the total impulse experienced at these locations. Figure 3.19 shows the maximum peak pressures across the head form and shows how a helmet reduces the maximum pressures near the ear, but also increases the maximum pressures near some of the pad locations.

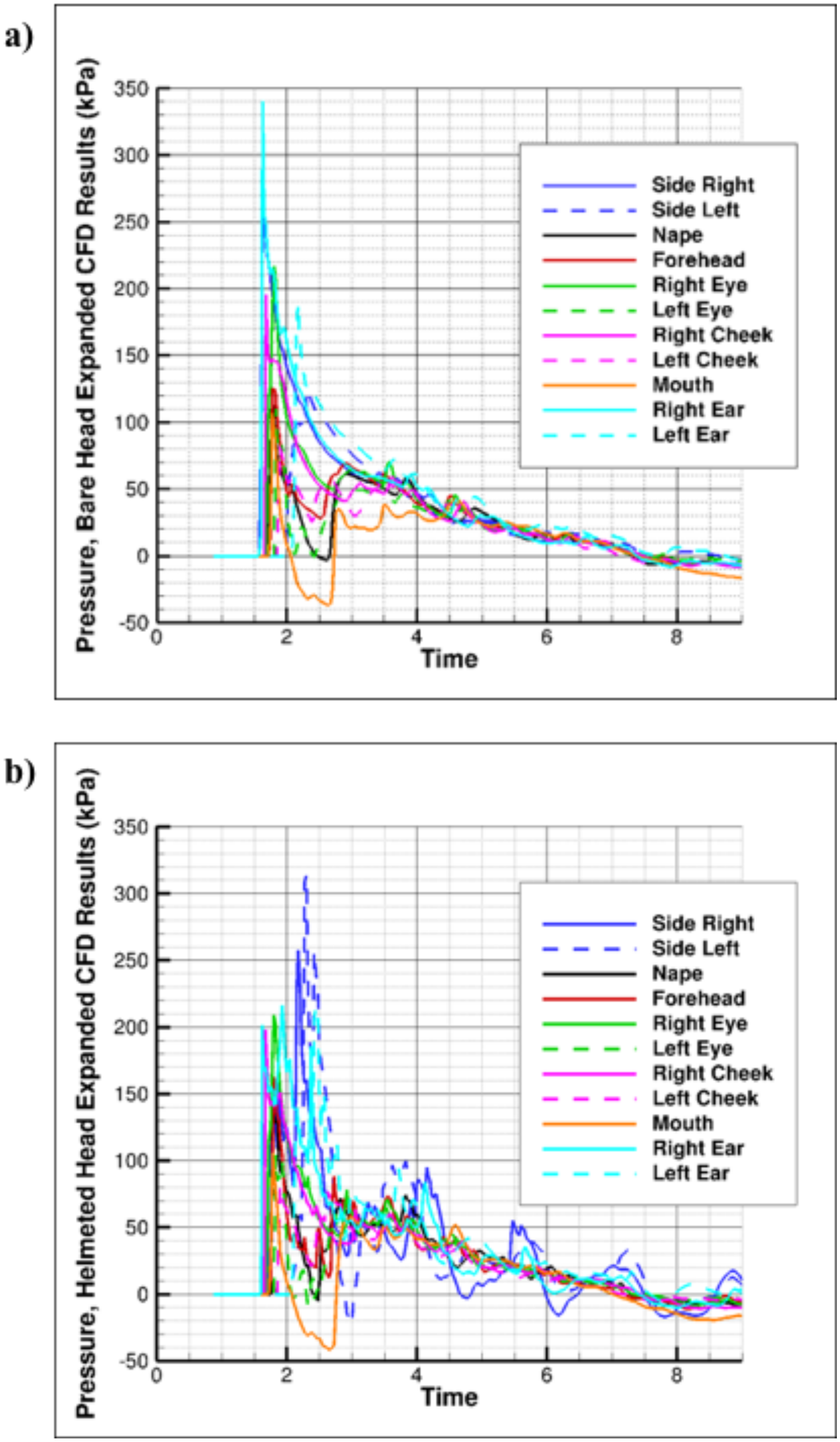

Figure 3.18: Additional CFD pressure time-history results for side impact

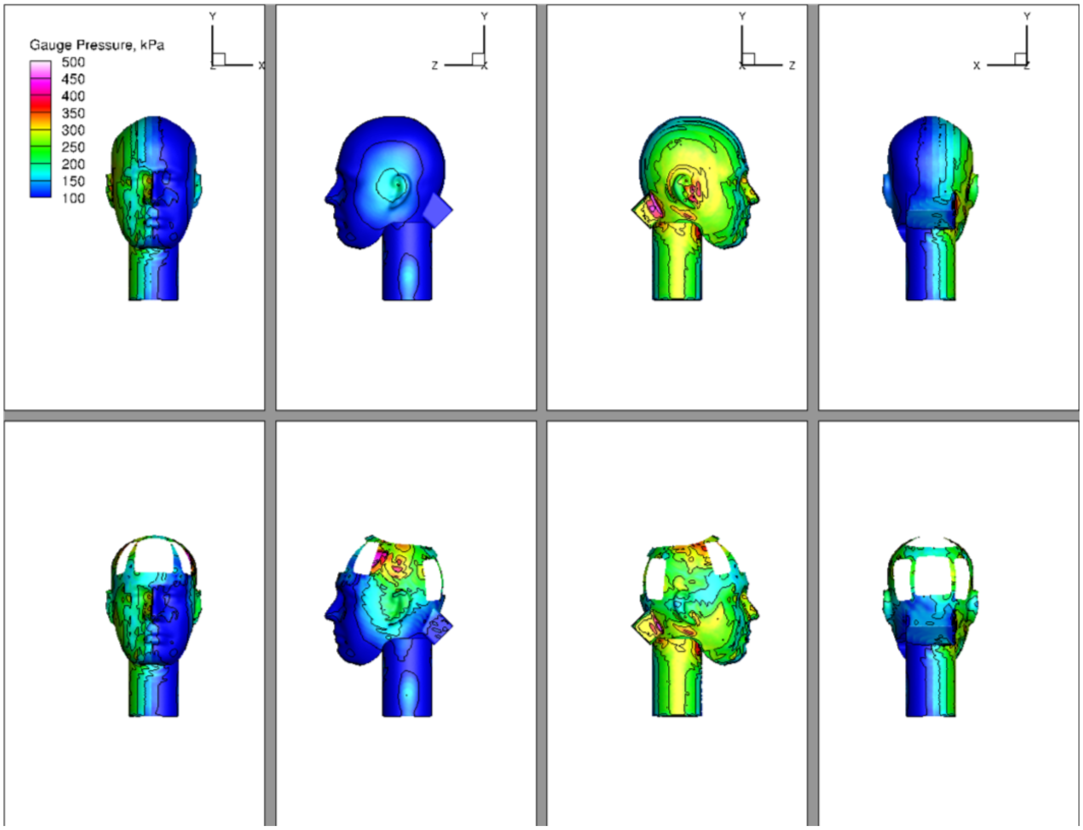

Figure 3.19: Maximum pressure observed for a side impact for bare and helmeted head form

3.3.3.3. Rear Impact

Figure 3.20 shows CFD predictions of the pressure-time history at both previously shown and additional locations around the bare and helmeted head forms for a rear impact. The peak pressures are significantly reduced at the locations being studied when the impact is to the back of the head. This result is expected because the back of the head is shaped in a manner which will tend to direct flow around itself rather than into a valley, as was observed with the eye sockets. Once again, the helmet clearly protects some areas of the head, evidenced by decreased peak pressures at the nape location. Similar to other impact orientations, the side right location (and side left location) experiences secondary pressure peaks, likely due to reflections between the head form and helmet.

The nape location’s sensor is near the data acquisition junction box, which makes this head form geometry less realistic. A future analysis should be done without the junction box modeled in order to understand whether this trends continue to hold. This CFD model included the junction box to best match the experimental geometry.

Figure 3.21 shows the maximum pressures on the head form. It is evident that most of the pressures are occurring in the cusp formed by the back of the head and the junction box. An analysis without the junction box would be needed to understand what the maximum pressure distribution would be for a real human head.

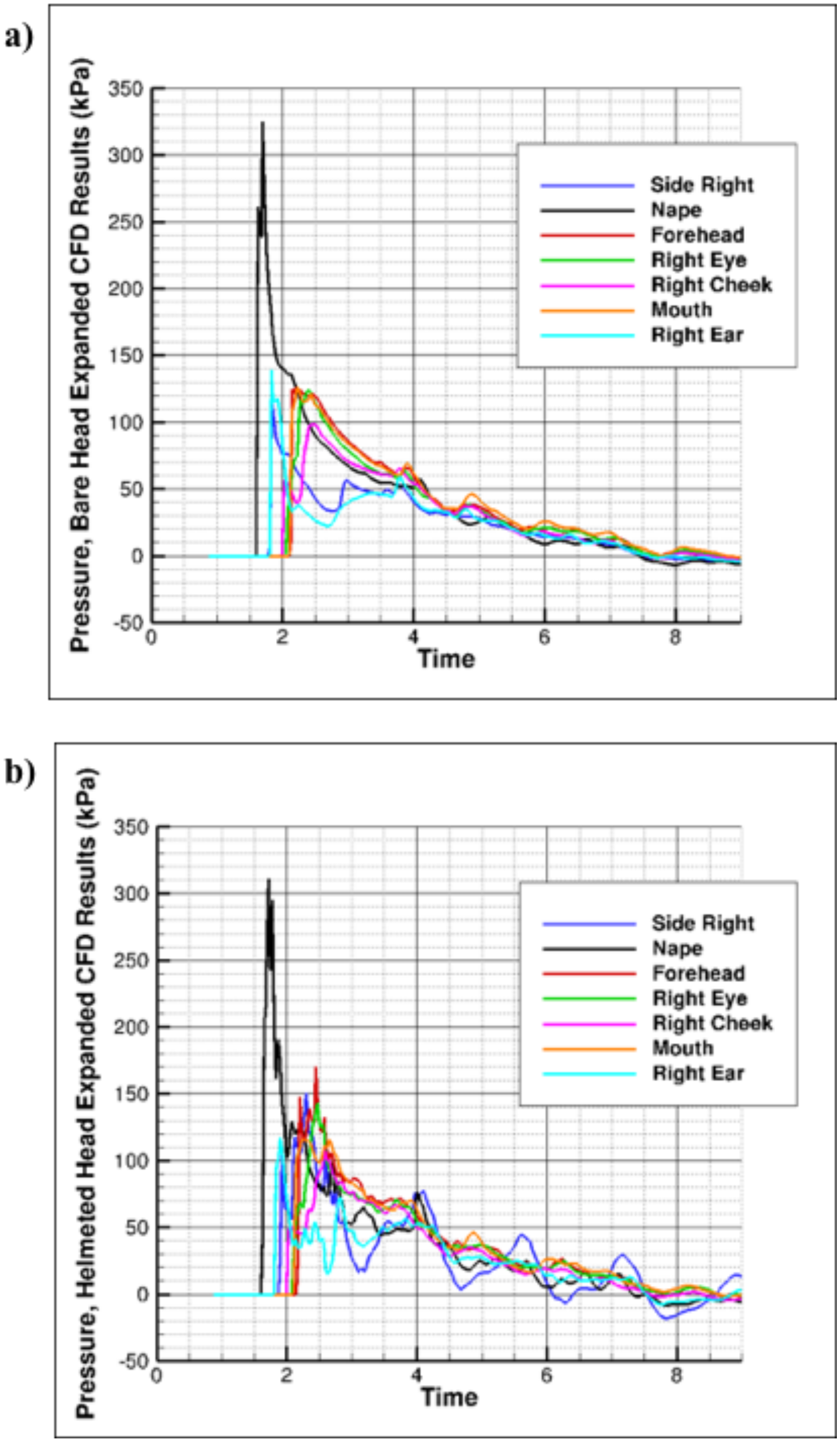

Figure 3.20: Additional CFD pressure time-history results for rear impact

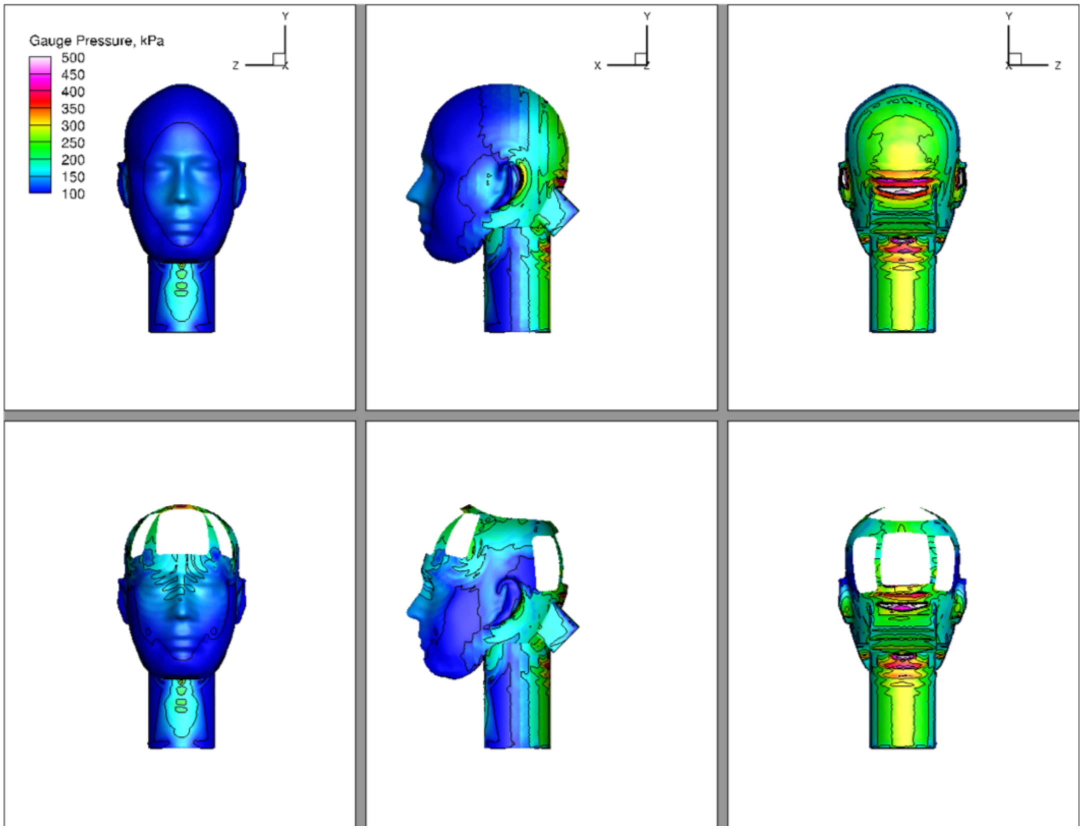

Figure 3.21: Maximum pressure observed for a rear impact for bare and helmeted head form

3.4. Discussion

The purpose of this paper was to use CFD simulations of bare and helmeted head models inside the JHU/APL BOSS to understand the impact of a nominal helmet design for different blast-impact orientations. Data from the CFD simulations were compared directly to experimental data from the shock tube experiments to validate the CFD process. General trends were compared to conclusions made by NRL through free-field tests of unprotected and protected head forms in different orientations.

A key finding of this work is that CFD models can accurately model the flow inside of a shock tube and the overpressures on the complex test article within it. Experimental and CFD data were found to agree within 20% for peak pressures and positive phase time duration at many of the studied locations representing a majority of the head form. This validation allows the use of future CFD simulations to gather data over the entire head surface instead of relying on select probe locations. For example, the total impulse to the head could be calculated from the CFD data to understand the impact of protective equipment in one metric.

From comparing the bare and helmeted head form data, it is clear that the helmet did not reduce the peak pressures at all locations, nor does it decrease the impulse at all locations. However, the helmet did reduce the peak pressure at many locations, depending on the blast-impact orientation. These trends are consistent with those observed in the study conducted by NRL when using free-field tests. Furthermore, the helmet does not negatively impact any exposed locations due to extraneous reflections. It is evident that both the side left and side right locations are affected by multiple reflections caused by the helmet, likely increasing total impulse at those locations.

Overall, the highest overpressures were observed at the eyes for a frontal impact with or without the helmet. This result can be explained by the natural geometric contours of the human face. This result also suggests that PPE such as goggles or visors may be beneficial. Future work should include a study of some key metrics such as total impulse on the head form for different combinations of PPE. Although NRL has already provided data on different combinations of PPE, the data were limited to pressure-time traces at specific locations. Additionally, the CFD model for this study should be used without the data acquisition junction box to improve the realism of the results in that area.

4. Summary of Research

CFD simulations were used to characterize the flow inside shock tubes and corroborate previous research that showed shock tubes can be used to replicate free-field blast waves. Then, CFD was used to study of the flow inside a custom shock tube built at JHU/APL. The CFD model was validated against available experimental data taken from shock tube wall pressure sensors and pressure sensors on test articles within the shock tube. The validated CFD model was then used to study the impact of helmets on head overpressures for different blast-impact orientations. The key results of this research are described below.

4.1.1. Using Gas-Driven Shock Tubes to Produce Blast Wave Signatures

In the first study, a CFD model of a constant area shock tube was created. Computational studies were performed to characterize the primary overpressure blast environment created by the shock tube design as the membrane burst pressure (implemented through a higher initial pressure in the driver section), driver length, and driving gas were parametrically varied. Prior research results, such as the production of flat-top waves with the use of air as a driving gas, were corroborated. A key finding of these studies was the confirmation of previous work showing that shock tubes can be used to generate blast waves. However, the studies also demonstrated that a pressure signature representative of a blast wave only existed for a short period of time and at a particular location within the shock tube. The location at which this pressure signature occurred varied with shock tube design parameters. The change in the pressure-time history was shown as a function of location for various CFD simulations to highlight how a certain setup could result in a blast wave that varied significantly depending on the test section location.

4.1.2. Assessment of Helmet Effectiveness against Blast Waves using Computational Fluid Dynamics Simulations of Gas-Driven Shock Tubes

In this study, a CFD model of the BOSS, a custom shock tube built at JHU/APL with a test-section cross-sectional area large enough to test head forms without wall interference effects, was created. The BOSS was specifically chosen due to the availability of experimental data of pressures along the shock tube walls and on test articles. The CFD model was first validated against pressure data along the shock tube walls from laboratory testing. Initial agreement between the CFD model and experimental data was improved through the implementation of a custom diaphragm rupture model. The diaphragm of the shock tube was modeled as a hemispherical curve by implementing a boundary condition along it. This model effectively increased the driver section's volume, which increased the peak pressure downstream the shock tube. Next, the CFD model was validated against pressure data measured by sensors on both bare and helmeted head forms. General agreement for pressures along the head form was worse than agreement for data measured on the shock tube wall, but peak pressure and positive phase durations were within 20% of the corresponding experimental data.

Once the CFD model was validated, a comprehensive study of shock tube flow and its impact on a head form inside the test section was performed. CFD simulations corroborated experimental data, which showed that the helmet did not always decrease overpressures at all locations. An effect known as “underwash” causes pressure in certain areas to increase because the gas is able to flow between the helmet and head, ultimately reflecting off pads under the helmet and onto the head. Simulations were conducted to show the effect of varying the impact orientation between the front, side, and rear. It was found that the highest overpressures on the head were at the eye sockets when the head directly faced the incoming blast wave. The helmet did not influence the pressures near the eyes, suggesting that goggles would be needed if the overpressures near the eyes could cause injury. Overall, impacts to the side or rear of the head resulted in higher overpressures for some locations along the head and lower overpressures elsewhere. The effects of the helmet were similar – overpressures were reduced in some areas while the total impulse was increased in some areas due to reflections.

4.2. Contributions to Modeling Blast Wave Exposures to the Human Head

The first contribution of this research was to corroborate that shock tubes can be used to replicate free-field blast waves by examining results from prior experimental research and demonstrating the feasibility and reliability of using shock tubes to replicate free-field blast waves. Prior research typically focused on a single location for the test section, whereas this work focused on the evolution of the blast wave as it traveled down the shock tube for all shock tube designs that were studied. The CFD simulations conducted as part of this thesis verified the experimental results, showcased the ability of CFD to accurately predict the shock tube physics in both time and space, and highlighted the sensitivity of the blast wave to test section location. As a result, this work enables researchers to use CFD to check the influence of a shock tube or experimental apparatus change prior to finalizing any major changes and conducting experiments. Furthermore, the results shown in this thesis highlight the need to look at the evolution of the blast as it travels downstream. The blast may not generate the desired pressure signature at one test section location, but it may generate a desired signature elsewhere.

The second contribution of this research was the development of a CFD model for a custom shock tube design. This work advances current knowledge through the development of a technique to model the diaphragm rupture to improve agreement between CFD and experimental data. Furthermore, grid and time independence studies were conducted to ensure good accuracy from the CFD model. Both wave speed and shock reflections were captured in the CFD model with sufficient accuracy relative to the experimental data. This CFD model enables researchers to rapidly run simulations to assess different protective equipment designs on test articles and quickly vary conditions to test different blast impact orientations. CFD predictions of shock tube designs and overpressures on head forms allow researchers to quickly and more thoroughly assess the impact of new concepts prior to collecting more time-consuming experimental data.

Prior experimental research using free-field testing found that some PPE lower the pressure experienced on parts of the head, while simultaneously increasing the pressure on experienced at other locations. This research also found that the same type of trends occurred when a CFD model of a shock tube was used to predict the overpressures on the modeled head form with a different helmet than was used in the previous research.

4.3. Suggestions for Future Work

This thesis focused on the use of CFD simulations that modeled the head forms as rigid bodies. Helmeted head forms were also modeled as single rigid bodies. Thus, the motions of the head forms and the helmets relative to the head forms were not modeled.

The overpressures predicted by the CFD simulations described in this research were then input into separate simulations that modeled head form dynamics, resulting in a decoupled approach. Coupling the head form motion with the CFD simulations such that the pressure informed the motion and the motion informed future pressures would be worthwhile future work.

Additionally, the CFD simulations were set up such that the helmet and the padding underneath the helmet were both set to wall boundary conditions with no porosity. In reality, the padding is likely to compress and deform as the head and helmet are impacted by the blast wave. Additionally, some of the gas will likely pass through the helmet and its padding instead of completely reflecting off of them. Modeling porosity may be a simple way to reduce and more accurately predict the magnitude of the overpressures caused by reflections from the helmet. A sensitivity study that compared computational results for different levels of porosity to experimental data could result in improved predictive capability when using CFD.

Finally, assessment of other forms of PPE, such as goggles and mandible protection would be beneficial. Understanding how various forms of PPE and their different designs impact the resulting overpressures could assist researchers with improve the design of PPE for the warfighter. CFD could be used to understand the reasons why certain PPE increases overpressures for specific regions of the head. This understanding could then influence alterations to the design of that PPE.

Finally, much of this research focused on larger diameter blast simulators, but not all research centers have the luxury of having systems with these larger diameters. Some prior research efforts have begun to characterize the effects of testing outside the end of a shock tube, called end-jet testing, and if the resulting blast wave is valid. However, researchers have drawn conflicting conclusions and most research efforts have focused on single shock tube designs. Fully characterizing when it is acceptable to conduct end-jet testing through a parametric study would be extremely valuable future work to enable laboratory and shock tube testing of test articles larger than the test sections.

5. References

[1] D. Warden, "Military TBI during the Iraq and Afghanistan wars," *The Journal of Head Trauma Rehabilitation,* vol. 21, no. 5, pp. 398-402, 2006.

[2] G. F. Kinney, Explosive Shocks in Air, New York, NY.: Springer-Verlag, 1985.

[3] W. E. Baker, Explosions in Air, Austin: University of Texas Press, 1973.

[4] A. C. Merkle, C. M. Carneal, I. D. Wing, A. C. Wickwire, J. M. Paulson, K. A. Ott, E. E. Ward, T. P. Harrigan, J. C. Roberts, B. G. Carkhuff and T. M. Taylor, "Biomechanics and Injury Mitigation Systems Program: An Overview of Human Models for Assessing Injury Risk in Blast, Ballistic, and Transportation Impact Scenarios," *JOHN HOPKINS APL Technical Digest,* vol. 31, no. 4, pp. 286-295, 2013.

[5] D. R. Mott, D. A. Schwer, T. R. Young, Jr. , J. Levine, J.-P. Dionne, A. Makris and G. Hubler, "BLAST-INDUCTED PRESSURE FIELDS BENEATH A MILITARY HELMET," in *Military Aspects of Blast and Shock*, Oslo, Norway, 2008.

[6] D. R. Mott, T. R. Young, Jr. and D. A. Schwer, "Blast Loading on the Head Under a Military Helmet: Effect of Face Shield and Mandible Protection," in *AIAA SciTech Forum*, National Harbor, 2014.

[7] C. E. Needham and G. Rule, "Laboratory Blast Testing Methodologies," in *29th International Symposium on Shock Waves 2*, vol. 2, R. Bonazza and D. Ranjan, Eds., Madison, Wisconsin: Springer, 2013, pp. 849-854.

[8] N. Chandra, S. Ganpule, N. Kleinschmit, R. Feng, A. Holmberg, A. Sundaramurthy, V. Selvan and A. Alai, "Evolution of blast wave profiles in simulated air blasts: experiment and computational modeling," *Shock Waves,* vol. 22, pp. 403-415, 2012.

[9] A. Sundaramurthy and N. Chandra, "A parametric approach to shape field-relevant blast wave profiles in compressed-gas drivern shock tube," *Frontiers in Neurology,* vol. 5, p. 253, 2014.

[10] D. V. Reneer, R. D. Hisel, J. M. Hoffman, R. J. Kryscio, B. T. Lusk and J. W. Geddes, "A Multi-Mode Shock Tube for Investigation of Blast-Induced Traumatric Brain Injury," *Journal of Neurotrauma,* vol. 28, pp. 95-104, 2011.

[11] M. Kuriakose, M. Skotak, A. Misistia, S. Kahali, A. Sundaramurthy and N. Chandra, "Tailoring the Blast Exposure Conditions in the Shock Tube for Generating Pure, Primary Shock Waves: The End Plate Facilitates Elimination of Secondary Loading of Specimen," *PLoS ONE,* vol. 11, no. 9, pp. 1-19, 2016.

[12] A. Yu, M. Panzer, B. Bigler, R. C. Wood, A. Alshareef, G., D. Meaney, B. Morrison III and C. Bass, "In vs. Out: Controversies in Shock Tube Blast Experiments," in *Personal Armour Systems Symposium*, 2014.

[13] S. Ganpule, L. Gu and N. Chandra, "MODELING SHOCK RESPONSE OF HELMETED HEAD USING FLUID STRUCTURE INTERACTION," in *16th US National Congress of Theoretical and Applied Mechanics*, State College, 2010.

[14] S. Ganpule, L. Gu, G. Cao and N. Chandra, "THE EFFECT OF SHOCK WAVE ON A HUMAN HEAD," in *Proceedings of the ASME 2009 International Mechanical Engineering Congress & Exposition*, Lake Buena Vista, 2009.

[15] S. Ganpule, A. Alai, E. Plougonven and N. Chandra, "Mechanics of blast loading on the head models in the study of traumatic brain injury using experimental and computational approaches," *Biomechanics and Modeling in Mechanobiology,* pp. 511-531, 2013.

[16] A. Sundaramurthy, A. Alai, S. Ganpule, A. Holmberg, E. Plougonven and N. Chandra, "Blast-Induced Biomechanical Loading of the Rat: An Experimental and Anatomically Accurate Computational Blast Injury Model," *Journal of Neurotrauma,* vol. 29, pp. 2352-2364, 2012.

[17] M. Rodríguez-Millán, L. B. Tan, K. M. Tse, H. P. Lee and M. H. Miguélez, "Effect of full helmet systems on human head responses under blast loading," *Materials and Design,* pp. 58-71, 2017.

[18] D. V. Ritzel and S. Parks, "Shock Tube Apparatus for Blast Wave Simulation". US Patent 9027383, 12 May 2015.

[19] W. Bleakney, D. K. Weimer and C. H. Fletcher, "The Shock Tube: A Facility for Investigations in Fluid Dynamics," *Review of Scientific Instruments,* vol. 20, no. 11, pp. 807-815, 1949.

[20] S. Chakravarthy, O. Peroomian and B. Seka, "Some internal flow applications of a unified-grid CFD methodology," in *AIAA, ASME, SAE, and ASEE, Joint Propulsion Conference and Exhibit*, Buena Vista, 1996.

[21] H. Wilbraham, "On a certain periodic function," *The Cambridge and Dublin Mathematical Journal,* vol. 3, pp. 198-201, 1848.

[22] W. J. Gibbs, "Fourier's Series," *Nature,* vol. 59, no. 1522, p. 200, 1898.

[23] W. J. Gibbs, "Fourier's Series," *Nature,* vol. 59, no. 1539, p. 606, 1899.

[24] H. Mizuno, K. Sawada and A. Sasoh, "Numerical Study of non-ideal diaphragm rupture in expansion tube," in *40th AIAA Aerospace Sciences Meeting & Exhibit*, Reno, 2002.

[25] T. Takahashi, K. Watanabe, A. Sasoh, H. Torikai and Q.-S. Yang, "Active Shock-tube-diaphragm Rupture with Laser Beam Irradiation," in *42nd AIAA Aerospace Sciences Meeting and Exhibit*, Reno, 2004.